AN ABSTRACT OF THE THESIS OF

Eric D. Truong for the degree of Honors Baccalaureate of Science in Mechanical Engineering presented on October 21, 2013. Title: Cryogenic Single-Phase Heat Transfer in a Microscale Pin Fin Heat Sink

Abstract approved:

_____

Vinod Narayanan

A combined experimental and computational fluid dynamics (CFD) study of single-phase liquid nitrogen flow through a microscale pin-fin heat sink is presented. Such cryogenic heat sinks could find use in applications such as high performance computing, spacecraft thermal management, and hydrogen storage thermal management. A circular pin fin heat sink in diameter $5\ cm$ and 250 micrometers in depth was studied herein. Unique features of the heat sink included its variable cross sectional area in the flow direction, variable pin diameters, as well as a circumferential distribution of fluid into the pin fin region. The stainless steel heat sink was fabricated using chemical etching and diffusion bonding. Experimental results indicate that the heat transfer coefficients were relatively unchanged around $2600\ W/m^2K$ for flow rates ranging from $2 - 4\ g/s$ while the pressure drop increased monotonically with the flow rate. None of the existing correlations in literature on cross flow over a tube bank or micro pin fin heat sinks were able to predict the experimental pressure drop and heat transfer characteristics. CFD was used to solved for the momentum and energy equations for a laminar flow, steady-state, with initial and boundary conditions. Commercial code, developed by ANSYS Fluent, was used to

perform the simulations. The three dimensional model showed reasonable (~7 percent difference) agreement in the average heat transfer coefficients between experiments and CFD simulations.

Key Words: heat transfer, heat sink, micro pin-fin, cryogenic cooling

Corresponding e-mail address: 3rictruong@gmail.com

Cryogenic Single-Phase Heat Transfer in a Microscale Pin Fin Heat Sink

by

Eric D. Truong

A PROJECT

submitted to

Oregon State University

University Honors College

in partial fulfillment of
the requirements for the
degree of

Honors Baccalaureate of Science in Mechanical Engineering (Honors Associate)

Presented October 21, 2013
Commencement June 2014

Honors Baccalaureate of Science in Mechanical Engineering project of Eric D. Truong presented on October 21, 2013.

APPROVED:

Mentor, representing Mechanical Engineering

Committee Member, representing Mechanical Engineering

Committee Member, representing Mechanical Engineering

Dean, University Honors College

I understand that my project will become part of the permanent collection of Oregon State University, University Honors College. My signature below authorizes release of my project to my reader upon request.

Eric D. Truong, Author

ACKNOWLEDGEMENTS

Foremost, the author would like to expresses his gratitude to Dr. Vinod Narayanan for the opportunity to be on the project. The patient and support he has shown have made the learning experience gratifying. The author especially wants to thank Dr. Vinod Narayanan for exemplifying the role model of hard work and dedication, who refuses to settle for good enough and expects nothing less of his students.

To friends and lab mates, the author would like to thank them for all their help and support. This project couldn't have been completed without their contributions. To Erfan Rasouli, who was an equal partner, if not more, on the project and was there throughout the whole process; to Mohammad Ghazvini and Shashank Natesh for imparting their knowledge on numerical simulation in ANSYS Fluent; and to Thomas L'Estrange who was kind enough to take on the daunting task of formatting and editing. The significant of their help and contributions are of equal weight in their own right, and listed in no particular order.

The author deepest appreciation goes out to my committee members, Dr. Apte Sourabh and Kevin Drost, who took time from their busy schedule to read and provided feedback on the document. Appreciation also goes to Dr. Deborah Pence and Dr. Kendra Sharp for their willingness to be on the committee but couldn't due to schedule conflicts.

Finally, financial support for the project is provided through the Hydrogen storage by the Department of Energy through grant number DE-FC36-09GO19005.

CONTRIBUTIONS OF AUTHORS

This thesis is an extended version from a conference paper coauthor by Erfan Rasouli and Dr. Vinod Narayanan. Specifically, Erfan wrote the experimental procedure in section 2.8, experimental data reduction and uncertainty analysis in chapter 3, and conclusion in chapter 6. Additionally, Erfan generated all the plots and provided photos taken of the experiments. Dr. Vinod Narayanan wrote the abstract, introduction and objectives in chapter 1, and results and discussion in chapter 5.

DEDICATION

The effort of this work is dedicated to the author's Mother and Sister, who have always been there, through good and bad, for support. The long hours put forth in effort were durable with them in mind.

TABLE OF CONTENTS

Page

TABLE OF CONTENTS (CONTINUED)

Page

LIST OF FIGURES

Figure Page

LIST OF FIGURES (CONTINUED)

Figure Page

LIST OF FIGURES (CONTINUED)

Figure Page

LIST OF FIGURES (CONTINUED)

Figure Page

LIST OF TABLES

Table Page

Cryogenic Single-Phase Heat Transfer in a Microscale Pin Fin Heat Sink

1. INTRODUCTION AND OBJECTIVES

The ever increasing requirements for heat dissipation in applications such as computer chip and high power electronics cooling have necessitated research in advanced high heat flux cooling technologies. Microchannel heat sinks have emerged as one of the promising technologies to meet this need. The high surface to volume ratio afforded by microchannels results in a high heat transfer rate to the fluid. Beginning with the pioneering work by Tuckerman and Pease [1], both single phase liquid flows as well as phase-change flows in microchannels have been studied over the past two decades and have been summarized in several review papers [for example, 2-4]. Various means to enhance heat transfer rates through microchannels have been investigated, including variations in flow geometries, substrate material and coolant fluids. Reduction of pressure drop through the microchannel heat sinks has also received considerable attention. Advances in micro fabrication and computational fluid dynamics (CFD) have provided the needed tools to gain better insight and help optimize the geometries of micro heat sinks for various applications.

Pin fin microchannel heat sink geometries have been studied over the past decade due to the potential for reduction in flow mal-distribution that could exist between parallel channels and reduced heat sink thermal resistance when compared with parallel microchannel arrays [5, 6]. Rubio-Jimenez et al. [5] performed an optimization study on four different fin geometries (circle, square, ellipse, and elongated circle) arranged on a silicon base with dimensions of $10mm$ x $10mm$. While holding the pin fin geometry

fixed, they also studied variation of pin height at a fixed density, and the pin density keeping other parameters fixed. Results showed that pin shape had a more pronounced effect on pressure drop than on the heat transfer rate. Elongated circle pins resulted in the lowest pressure drop amongst the compared geometries. Variable pin density arrangements were able to maintain uniform temperature at the base to within $6\ °C$ for the input heat flux of $100W/cm2$ at a flow rate of $1ml/s$. Two parallel microchannel heat sinks were also simulated at the same heat flux and mass flow rate for comparison. It was reported that the thermal resistance of the parallel channels was four times larger than the micro pin fin heat sink with variable pin density.

Tullius et al. [6] numerically studied the effect of pin parameters on single phase flow and heat transfer rate in microchannel pin fin heat sinks and compared the pin fin heat sink performance with parallel microchannel heat sink. The variables in their study included 1) pin sizes which ranged from 500 to $1000\mu m$, 2) pin geometry (circle, square, triangle, ellipse, diamond, and hexagon), 3) pin width to channel height ratio, 4) pin width to spacing, and 5) pins material (carbon nanotubes, silicon, copper, and aluminum). They reported that at high Reynolds number (Re), triangular pin fin heat sink achieved the highest Nusselt number (Nu), while circular and elliptical pins showed the lowest Nu. Nevertheless, they noted that the Nu for elliptical and circular pin fins were 45% higher than that for parallel channels. Heat sinks with square pins of $500\ \mu m$ side showed an 88 percent increase in Nu with a 15 percent increase in pressure drop when compared with a parallel channel heat sink. Nu and pressure drop were found to increase with increase in pin height and with reduction in fin width and spacing. Fin material was found to have little effect on the thermal performance of the heat sink.

Experimental data of single phase flow through micro pin-fin heat sinks have led researchers to conclude that conventional correlations developed for macroscale heat exchangers cannot accurately predict heat transfer rate and pressure drop in such heat sinks. Koşar and Peles [7, 8] experimentally investigated flow and heat transfer rate through a staggered circular pin-fin channels made from silicon wafer with peak-to-peak roughness of $\sim 0.3\mu m$. The pin had diameter of $99.5\ \mu m$ and height of $243\ \mu m$ for two fluids- deionized water and R-123. Reynolds numbers, based on the pin diameter, ranged from 14 to 112 for deionized water [7] and from 134 to 314 for R-123 [8]. They reported a transition point, $Re = 50$ for the case of water and $Re = 100$ for refrigerant, below which macroscale correlations could not predict the pressure drop and heat transfer trends. For water [7], the macroscale heat transfer correlations and correlations for millimeter sized pin fins did not agree with measured data. However, Zhukauskas correlation was able to predict the R-123 [8] data to within 15.5%. The authors attributed the differences between the correlations and their data to the boundary layer growth at the end walls of the pin fins, which are not taken into account in correlations for cross flow over a tube bank. A heat transfer correlation was developed to predict water and R-123 data to within 9% and 16.1% [8], respectively. Prasher et al. [9] conducted an experimental parametric study of hydraulic and thermal performance of an array of staggered square and circular pin-fins with water as the working fluid. Pin diameters ranged from 50 to $150\mu m$ and aspect ratio, H/d, varied from 1.3 to 2.8, while the Re ranged from 40 to 1000. They noted that a Re =100 separated two regimes which were described by two separate correlations. In contrast with observations by Koşar and Peles [7, 8], Prasher et al. [9] did not find any existing macroscale correlations to match their

data at the higher Re and hence proposed new correlations. Siu-Ho et al. [10], Qu and Siu-Ho [11, 12] studied water flow across an array of staggered square pin-fins with a cross section of 200 x $200\mu m$ and a height of $670\mu m$ for Re ranging from 93 to 634 [10] and 46 to 180 [11, 12] respectively. Siu-Ho et al. [10] reported that their data agreed with Moores and Joshi's [13] correlation for friction factor in the Re range of 93-624. However, when comparing their heat transfer data against 8 existing correlations developed for long, intermediate, and micro pin-fins, Qu and Siu-Ho [11] noted that the smallest mean average error between their data and correlations was at best 71 percent. In the second part of the study focused on low Re from 46-180, Qu and Siu-Ho [12] noted that the experimental pressure drop could not be well represented by existing correlations, including that by Moores and Joshi [13]. Based on their experimental studies, Qu and Siu-Ho [11, 12] proposed new correlations for heat transfer and friction factor for the low Re range. From this review of experimental microscale pin fin heat sink studies, it can be summarized that not only have conventional correlations failed to fully predict the thermal and hydrodynamic behaviors in micro pin-fins, but that correlations developed by one group have not been found to predict data by other groups.

Numerical simulations have provided an additional tool to analyze and validate experimental data for studies of fluid and thermal characteristics in micro pin-fin arrays. Konishi et al. performed a CFD study on the geometry experimentally tested by Siu-Ho et al. [10], Qu and Siu-Ho [11, 12] for a mass flow rate ranging from 181 to $1649\ kg/m2s$. Whereas the experimental data were compared with 11 friction factor correlations without a satisfying match, they showed good concurrence with numerical results for Re below 700. Following the work of Konishi et al. [14], Mita et al. [15]

investigated the pressure drop of water flow across an array of staggered circular pin-fins of 180 μm diameter and 683 μm height for a mass flow rate ranging from 159 to1475 $kg/m2s$. The friction factor obtained from the experiment could not be predicted by existing correlations or by their CFD simulations.

The working fluids used to study the thermal and hydrodynamic characteristics of single-phase flow through microchannels such as water, refrigerants, and oils, exist in the fluid state at room temperature. Cryogenic fluids, also known as cryogens, are liquefied gases that exist in the liquid state at very low temperatures (less than $\sim 123\,K$). Cryogenic fluids are used widely in several applications such as in rocket engines as fuel and oxidizer, regenerative cooling of rocket engine combustor liners, missile warning receivers, in satellite tracking systems and in cryo-adsorbent hydrogen storage systems. The present work discusses cryogenic cooling relevant to computer chip cooling applications. While inherently inefficient and costly, cryogenic cooling using liquid nitrogen of computer chips offers some advantages. Liquid nitrogen has been used to cool supercomputer chips such as the ETA-10 due to the potential to double the speed of CMOS circuit chips [16]. In addition to that, the electrical and thermal resistivity of copper interconnects in the PCB decrease by about 5.6 times and by 1.4 times respectively with a decrease in temperature from $300K$ to $80K$ [16]. The advent of high temperature superconductivity (HTS) has created additional relevance for considering cryogenic cooling of electronic components that combine CMOS chips with superconducting interconnects [17]. Typically, the computer boards are directly immersed within the cryogenic fluid in order to eliminate thermal resistances from the heat source to the heat sink. In an immersion cooling context, Anderson et al. [17] presented an

optimization of cryogenically cooled computer board dissipating an average flux of $0.4\ W/cm^2$ using immersion cooling. They reported that saturated liquid nitrogen pool boiling systems would be capable of removing about 15 W/cm^2. Carlson et al. [16] were able to attain about $12\ W/cm2$ in the nucleate boiling regime with an immersion scheme with surface temperatures of $90K$. Anderson et al. [17] reported an increase of up to 30 percent in critical heat flux using subcooled pool boiling over saturated pool boiling of liquid nitrogen, although the system costs increased significantly due to a need to subcool the fluid.

Limited published literature exists on single and phase change heat transfer within microtubes and microchannels. Qi et al. [18] investigated the pressure drop and heat transfer characteristics for $1\text{x}10^4 < Re < 9\text{x}10^4$ with four $250\ mm$ long tubes with different diameters of $0.531mm$, $0.834mm$, $1.042mm$, and $1.931mm$. The authors reported that modified Colebrook and Gnielinski correlations can be used to predict experimental results with proper account for the surface roughness. They found that, because of the lower viscosity, the pressure drop decreased with increasing temperature. The local heat transfer coefficient decreased with increasing heat input due to a decrease in thermal conductivity.

1.2 OBJECTIVES

Based on literature review presented in the previous section, it is seen that there has been no work in published literature on single phase cryogenic cooling within microchannel heat sinks. Such a configuration can be considered as an alternative to direct immersion cooling in order to remove higher heat fluxes. Based on the advantages summarized by the aforementioned studies, a pin fin microchannel heat sink was chosen

for the study. Unlike the other studies, the heat sink used in the present study differed in geometry from traditional pin fin heat sinks and was governed by requirements of the application of removing heat from a circular cryogenic vessel. The pin fin heat sink geometry and the unique features are described in the next chapter. The objectives of this study are to:

(a) Experimentally characterize the single-phase heat transfer rate and pressure drop in microscale pin fin heat sinks,
(b) Assess the applicability of existing correlations of pressure drop and heat transfer rate in literature to predict the experimental data and
(c) Develop 3D CFD simulations to determine pressure drop and heat transfer rate and compare the experimental data with simulations.

Given the lack of parity between the macroscale correlations in literature on microchannel pin fin heat sinks from the previous section, it was anticipated that a 3D CFD simulation would be needed to predict the experimental results.

In order to accomplish the first objective the following tasks were needed:

1. Design and development of an experimental facility for cryogenic flows, including a safety plan
2. Debugging of the experimental facility to permit establishment of stable operating conditions
3. Fabrication of the microscale pin fin heat sink
4. Experimental testing of pressure drop and heat transfer rates
5. Data reduction and analysis

2. EXPERIMENTAL FACILITY

This chapter provide details on the microchannel test section and test facility design followed by preliminary test procedures and data analysis that are to be followed during different stages of the experiment.

2.1 MICROCHANNEL HEAT SINK

Flow and heat transfer in a uniquely structured microchannel heat sink is presented in this paper. The heat sink was designed by other team members at OSU working on the project and is indented to be inserted into a circular vessel containing adsorbent material. The pin fin heat sink design, shown in Fig. 1, is different from current designs of micro pin fins in three respects. Firstly, that the heat sink is circular in plan form compared with the typical rectangular pin fin heat sinks presented in literature. Fluidic inlet and exit tubes are located on either ends of the circular microchannel heat sink and flow is distributed into the pin fins via an outer ring of tabs. The second distinction is that the heat sink incorporates heterogeneity in pin fin diameters. Three pin diameters of $0.5mm$, $1.3mm$, and $2mm$ corresponding to a pin height to diameter ratio of 0.5, 0.2, and 0.125 respectively were distributed within the heat sink. Seventy one percent of the pins were of $0.5mm$ diameter while 24 percent of the pins were of diameter $1.3mm$. Only 10 pins (4 percent) were of $2mm$ diameter; these pins were originally intended for local temperature measurement within the heat sink. The third distinction is that pins were distributed in a radially symmetric fashion with a radial spacing of $2.5mm$ and a circumferential arc length separation of $\sim 2.4mm$.

The internal flow path of the heat sink, shown in Fig. 2, was fabricated out of a 7-cm diameter $0.5mm$ stainless steel 316 shim that was etched to a depth of $0.25mm$ over a diameter of $5cm$. The diameter of the tab circle within which pin fins are located, was $40mm$. The average surface roughness, Ra, of the bottom surface of the etched heat sink was measured using an optical profilometer, to be $4\mu m$. A $250\mu m$ thick top plate with 2-mm inlet and exit holes was diffusion bonded to the etched plate to form the microchannel heat sink. Fig. 2 shows the top and bottom plates of the etched heat sink.

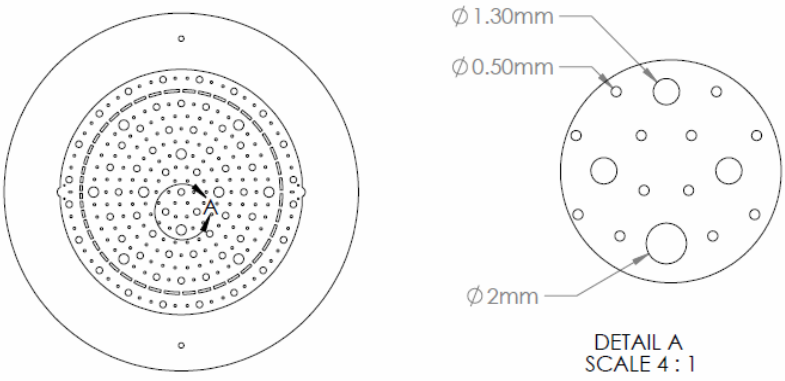

Figure 1. Top view of the microchannel pin fin heat sink with detail of the variable diameter of pin fins.

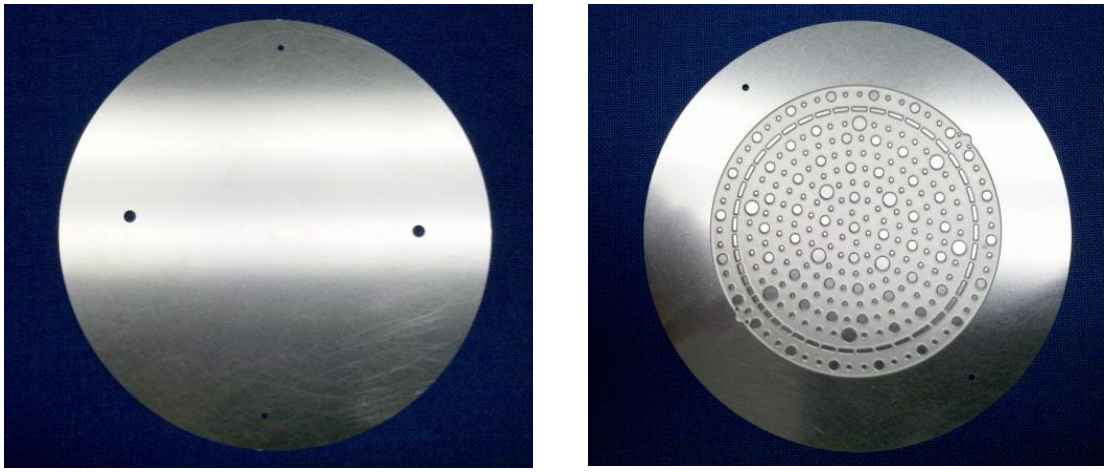

(a) *(b)*

Figure 2. Microchannel cooling plate (a) top plate showing holes for headers and alignment, (b) bottom plate with etched Microchannel and pin fins.

Due to the circular geometry, the cross-sectional area for flow from the inlet to exit within the heat sink was variable, resulting in variations in cross-sectional velocity through the heat sink. Fig. 2 shows the variation in the local Reynolds number,

$$Re_{local} = \frac{\vec{v}_{local} D_{h,local}}{\nu} \tag{1}$$

as a function of the scaled distance along the microchannel, x/D. In Eq. 1, the local cross-sectionally averaged velocity, $\vec{v}_{local}$was determined as

$$\vec{v}_{local} = \frac{\dot{m}}{\rho A_{c,local}} \tag{2}$$

and the local hydraulic diameter was determined as

$$D_{h,local} = \frac{4A_{c,local}}{P_{w,local}} \tag{3}$$

where $P_{w,local}$ is the wetted perimeter at the local cross section under consideration. The two curves in Fig. 3 represent the highest flow rate and lowest flow rate used in the experimental study. The smaller area at the inlet and exit ports act as diverging and converging sections, respectively, resulting in an increase in Re at these locations as a result of an increase in velocity. The Re ranges from 3200 to 1500 in the range of flow rates studied in the inlet and exit sections. However, from x/D of 0.15 to about 0.8, the Re was approximately constant and independent of x/D for a fixed mass flow rate, indicating that the increase in cross-sectional area and decrease in cross-sectional velocity were proportional to each other. With the exception of the conditions at the inlet and exit, the flow throughout the channels remained under 2000, and hence laminar flow was assumed in the CFD simulations described later. Since the Re was constant along a large fraction of the heat sink, the average Re between 0.15 and 0.8, $\overline{Re}$, used in reporting experimental data for this heat sink.

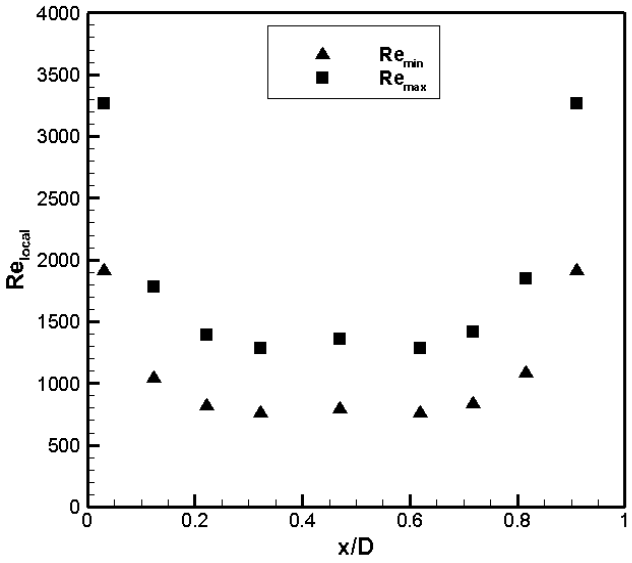

Figure 3. Variation of local Re along the heat sink vs. scaled distance along the microchannel

The average Reynolds number, $\overline{Re}$, within the heat sink was based on an average of the Re_{local} (determined using Eq. 1) from x/D = 0.15 to 0.8.

2.2 EXPERIMENTAL DESIGN

2.2.1 TEST SECTION DESIGN

The goal of the experiments was to quantify heat transfer rates and pressure drop in single-phase liquid nitrogen flows in a pin-fin microchannel heat sink. Characterization of heat transfer rates was conducted as a function of flow velocity by determination of the heat transfer coefficient. In non-dimensional terms, the single-phase experiments seek to provide a relationship between Nusselt number (Nu) and Reynolds number (Re), and between friction factor (f) and Re for liquid nitrogen flow through the microchannel

cooling plate. The obtained heat transfer rate and pressure drop data was used to validate the detailed CFD simulations using ANSYS FLUENT.

In order to characterize the single-phase pressure drop and heat transfer for the heat sink in Fig. 1, the friction factor and Nu was determined for various Re.

The pressure drop represented non-dimensionally in terms of the friction factor;

$$f = \frac{\Delta p(\bar{D}_h/\bar{L}_c)}{\rho\vec{v}^2/2} \tag{4}$$

where $\bar{D}_h$ and $\vec{v}$ are based on the average hydraulic diameter and cross-sectional velocity between x/D of 0.15 and 0.8. The characteristic length, $\bar{L}_c$ was determined as:

$$\bar{L}_c = \frac{\forall_{hs}}{\bar{A}_c} \tag{5}$$

where $\forall_{hs}$ refers to the fluid volume within the heat sink and $\bar{A}_c$refers to the averaged cross sectional fluid area between x/D = 0.15 and 0.8.

The area-averaged $\overline{Nu}$ was determined using

$$\overline{Nu} = \frac{\bar{h}\bar{D}_h}{k_f} \tag{6}$$

where $\bar{h}$ is the area-averaged heat transfer coefficient and k_f is the fluid thermal conductivity (determined using EES).

The area-averaged heat transfer coefficient was determined from the local heat transfer coefficient using

$$\bar{h} = \frac{1}{A_s}\sum_{i=1}^{n} h_{L,i}\, A_{L,i} \tag{7}$$

where L denotes a section of the heat sink, and A_s is the heated surface area of the heat sink. The sectional heat transfer coefficient was determined using Newton's law of cooling,

$$h_L = \frac{q_L^{"}}{(T_{w,L} - T_{b,L})} \tag{8}$$

where $q_L^{"}$ denotes the heat flux in that section, $T_{w,L}$ denotes the wall temperature in that section, and $T_{b,L}$ denotes the bulk fluid temperature in that section.

In order to determine h_L, in Eq. 8, local heat flux, local wall temperature and local bulk fluid temperature need to be known. The local bulk fluid temperature was determined using local energy balance,

$$T_{b,L,out} = T_{b,L,in} + \frac{q_L^{"} A_L}{\dot{m} c_{p,f}} \tag{9}$$

The bulk fluid temperature in section L is given by an average between $T_{b,L,in}$ and $T_{b,L,out}$ in Eq. 9. For the first section, the inlet temperature corresponds to the bulk fluid inlet temperature into the heat sink. Similarly, for the last section, the exit temperature is the heat sink fluid exit temperature.

Based on the above data analysis discussion, the following parameters need to be estimated in the experiments:

a. Pressure drop across the heat sink (ΔP)
b. Sectional heat flux, $q_L^{"}$
c. Sectional heat sink wall temperature, $T_{w,L}$
d. Heat sink inlet and exit bulk fluid temperatures $T_{b,in}$ and $T_{b,out}$
e. Mass flow rate, $\dot{m}$

Parameters a, d and e was measured using a pressure transducer, thermocouples, and a mass flowmeter, respectively. The sectional heat flux and wall temperatures were determined using a heat fluxmeter described below.

The heat fluxmeter consists of a piece of metal whose thermal conductivity is well characterized. Thermocouples are located vertically along the fluxmeter at known distances apart. The sides of the fluxmeter are insulated so that a 1-D heat flow can be approximated. Using the steady-state 1-D conduction equation, the heat flux is then determined based on the difference between the recorded temperatures at the vertical locations (ΔT), distance between the thermocouples (Δx) and thermal conductivity of the material (k)

$$q_L^{"} = -k\frac{\Delta T}{\Delta x} \tag{10}$$

The above equation was used to extrapolate to the microchannel surface temperature, T_w. Fig. 4 shows the dimensions of the $50mm$ diameter cylindrical fluxmeter in its side view. In order to obtain sectional heat flux and temperature measurements, the heat fluxmeter for this test section was segmented into three parts as shown in Fig. 4. An insulator was filled in between the three sections to ensure one-dimensional heat flux in the vertical orientation. Based on the needed heater power, space constraints, and thermal conductivity data from literature, titanium was chosen as the material for the fluxmeter. Thermocouples were located in the two blind holes in each segment of the fluxmeter. These thermocouples were spaced $20mm$ apart based on a

design stage uncertainty analysis for the heat flux. As shown in Fig. 4, two insulating blocks were located on the ends of the fluxmeter to ensure one dimensional heat transfer.

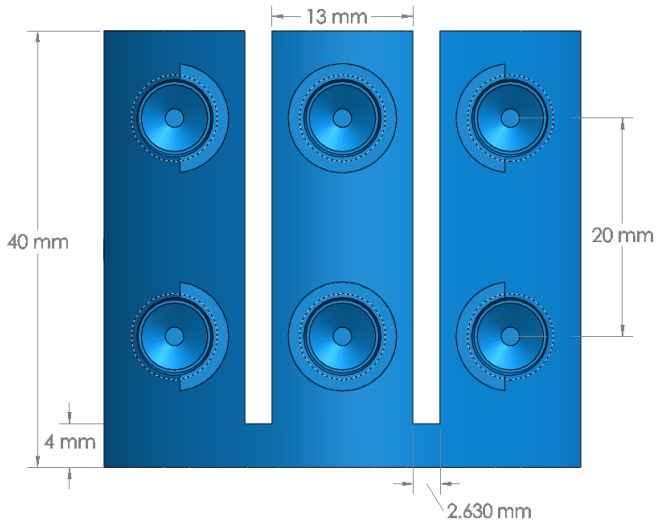

Figure 4. Schematic front view of the heat fluxmeter

In order to determine the distance needed between the heater located at the bottom of the fluxmeter and the lower thermocouple in Fig. 4, a 2-D simulation was performed using ANSYS FLUENT. Fig. 5 shows the simulation with an upper boundary condition of convective heat transfer coefficient that is typical of what will be seen with the microchannel flow. The side walls were insulated and a constant heat flux boundary is prescribed on the bottom wall of the fluxmeter. As seen from the temperature contours in Fig. 5, a 1-D heat flow can be assumed at the location of the bottom thermocouples.

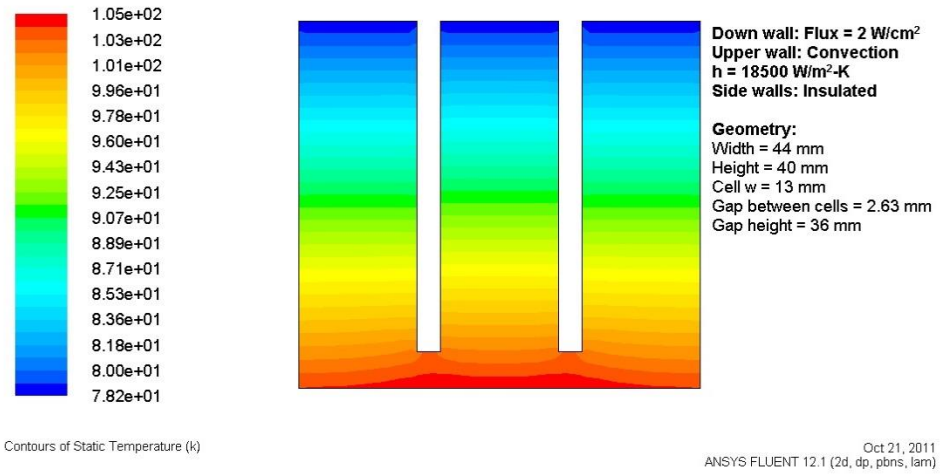

Figure 5. 2-D simulation of fluxmeter used ANSYS FLUENT to determine the dimensions of the fluxmeter

The test section was designed keeping in mind the variables that need to be measured with the lowest possible uncertainty (see section 3.2 for details on uncertainty estimates). Parasitic heat losses and material compatibility are of particular concern in the design of a cryogenic test facility. Fig. 6 shows an exploded view and Fig. 7 shows an assembled view of the final test section. The test section consists of a central microchannel cooling plate with an upper insulated header that supplies fluid, and a lower heat fluxmeter that supplies heat and measures both heat flux and wall temperature. A 400-watt square thick film heater, located at the bottom end of the heat fluxmeter, was used to provide thermal energy to the test section. Circumferentially located bolts hold all components of the test section together.

To minimize radial heat loss from the fluxmeter, cylindrical teflon insulation was used to completely enclose the fluxmeter. In addition, because of temperature difference between inside and outside of the insulation there still is a potentiality for radial heat loss. So as a second step, a guard heater was used around the insulation to provide a local

environment with temperature close to the inside. To quantify the required power of guard heater, the temperature difference between inner and outer sides of insulation need to be determined. The inner insulation temperature was determined by a mean average of the six thermocouples in the heat fluxmeter assumed while three surface thermocouples located on the outside surface of the insulation provide a representative of outer temperature. By using the guard heaters, the temperature difference between the inner and outer sides of the insulation would be balanced thereby yielding a1-D conduction through the fluxmeter.

The entire test section shown in Figs. 6 and 7 in the exploded and assembled views respectively. In these figures the guard heater is not shown. The test section is to be contained within an outer aluminum cylinder casing, which was in turn immersed within liquid nitrogen in a dewar. The test section is immersed in the dewar containing liquid nitrogen to reduce parasitic heat loss to the environment. The outer aluminum cylinder have interconnects for the inlet and exit flow as well as an interconnect for the thermocouples and heater wires.

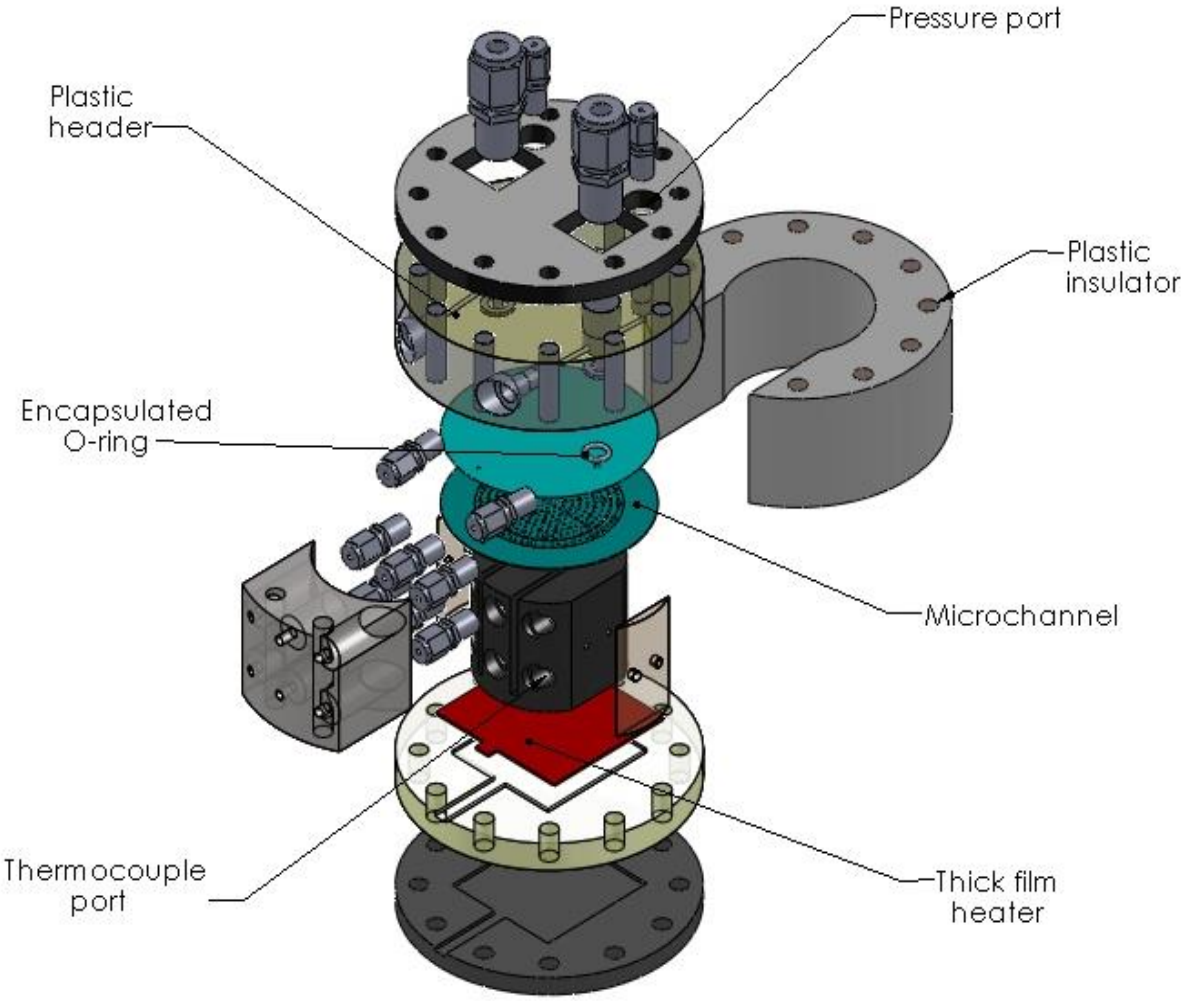

Figure 6. Exploded view of the test section

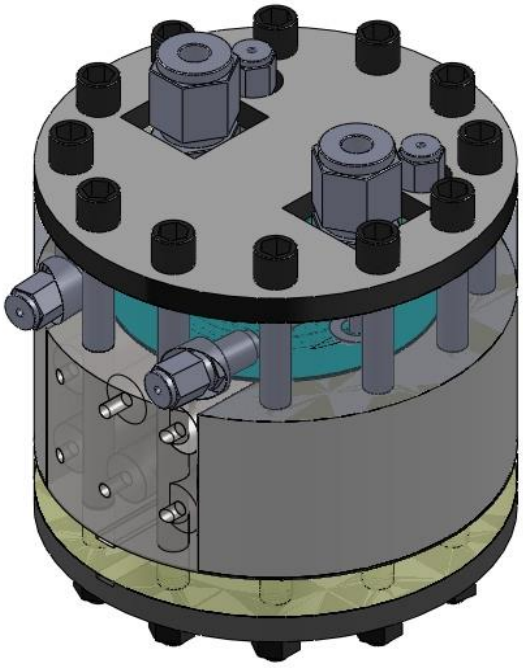

Figure 7. Assembled view of the test section

The upper header of the test section is shown in detail in Fig. 8. It is made using PCTFE plastic that is compatible with liquid nitrogen and cryogenic temperatures. Pressure and temperature were measured at the inlet and exit ports in order to accurately determine the pressure drop and bulk fluid temperatures. Fluid sealing between the header ports and the microchannel cooling plate was accomplished using encapsulated o-rings (FEP/Teflon encapsulated Viton) that are rated for cryogenic temperatures.

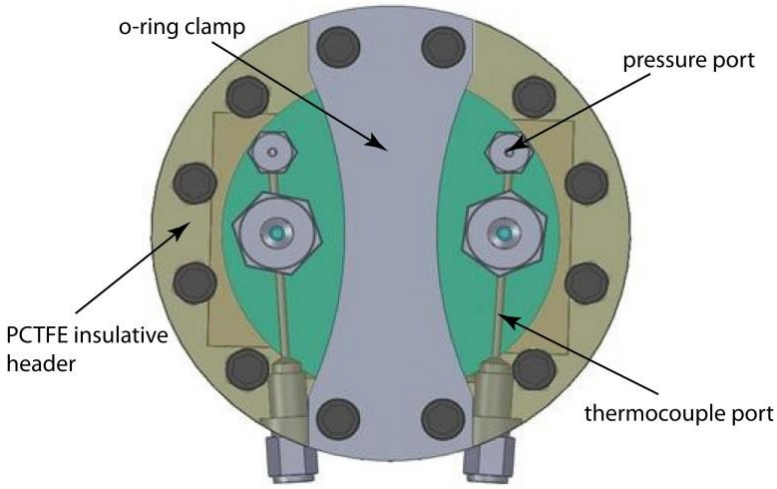

Figure 8. Schematic of the PCTFE header

Note that the initial intent of the test section design was to permit a constant heat flux boundary condition from both top and bottom sides of the microchannel heat sink. In order to do so, it would have been necessary to have fluidic interconnects as well as another fluxmeter on the top side. However, space restrictions did not permit such a design and hence constant heat flux boundary condition on one side was instead chosen, with the top side being an insulated boundary.

2.2.2 Experimental Facility Design

An experimental facility is needed to supply the fluid to the heat sink at the desired temperature and flow rates. Additional equipment is needed to maintain the requisite boundary conditions. Instrumentation is needed to measure the variables listed in the previous section. The measured flow parameters and their design ranges are provided in Table 1. A test facility needed to deliver the desired inputs to the test section

as well as to measure the variables with low uncertainty is shown in Fig. 9. Several safety features have also been incorporated into the test facility design. Table 2 provides a listing of the equipment and instrumentation present in the test facility.

Table 1. Measured variables and their anticipated range

Liquid mass flow rate (g/s)	$0.5 - 4$
Gas flow rate corresponding to above (at STP, l/min)	$24 - 192$
Differential pressure of μ-CHX kPa (psi)	$6.8 - 328$ $(1 - 47.6)$
LN_2 operating temperature (K)	$77 - 90$
Fluxmeter max. temperature (K)	320
Cryogenic-Cyl pressure range (bar)	$5 - 8$
Heating power (W)	$30 - 300$

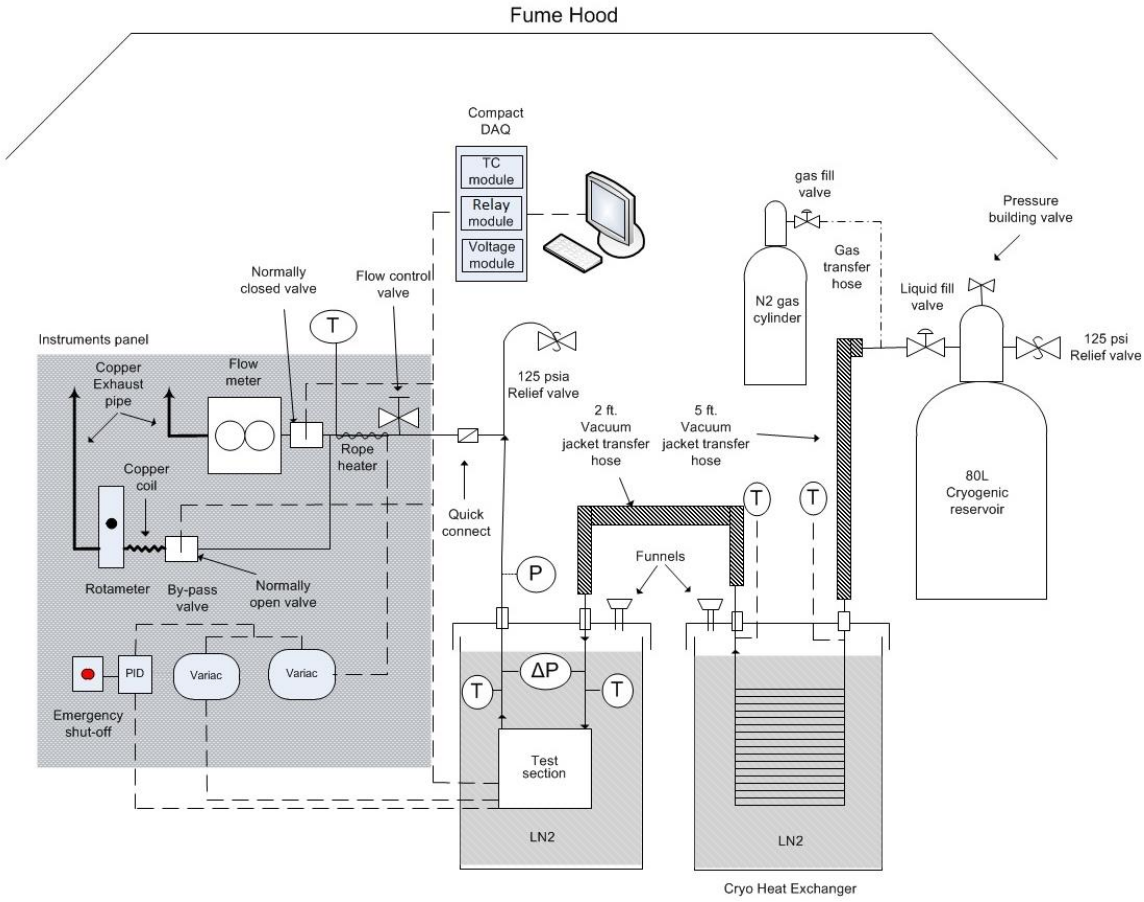

Figure 9. Schematic of the separate effects test facility

The test facility consists of an 80 liter cryogenic tank (cryocyl) that can be pressurized up to ~ 8 bar using a pressure building mechanism. The liquid will be at saturation temperature at the corresponding pressure within the tank. The fluid pressure in the tank is used to drive liquid nitrogen through the test facility (as opposed to use of a cryogenic pump). For single-phase experiments, the inlet temperature to the microchannel needs to be maintained subcooled for the given pressure. In order to accomplish subcooling of LN_2 at the set system pressure, a custom cryogenic heat exchanger is used. The heat exchanger consists of a coiled stainless steel tube immersed

in a dewar of LN_2. Since the pressure of LN_2 in the tube is higher than that in the dewar, subcooled LN_2 is expected at the exit of the heat exchanger. A second low-pressure 160 liter cryogenic tank was used to fill the dewar using a flexible hose and phase separator as shown in the Fig. 10. Temperatures were recorded at the inlet and exit of the heat exchanger to verify the subcooling. Liquid nitrogen then enters the test section that is located with a second (test section) dewar that contains liquid nitrogen. This dewar will also be filled using the 160 liter tank and transfer hose. A sliding mechanism was used to move the transfer hose from one dewar to the other, as illustrated in Fig. 10.

Temperatures at the inlet and exit of the test section, as well as the pressure drop across the test section were measured. An absolute pressure transducer was used to record the system pressure downstream of the test section dewar. A variac was used to supply controlled electrical power to the thick film heater in the test section. A manual Hoke cryogenic flow control valve was used to fix the flow rate through the test section. The flow rate was measured using an accurate gas flowmeter (Brooks Instruments), which requires an inlet fluid temperature of 20℃. Hence, LN_2 needs to be vaporized and brought to temperature following the flow valve and prior to the flowmeter. The heating was accomplished using a rope heater wound to the walls of the tubing. In order to prevent LN_2 from flowing into the flowmeter during start up, a flowmeter bypass loop is needed. A normally closed solenoid valve is located upstream of the flowmeter while a normally open solenoid valve is located in the bypass loop. The bypass loop also contains coiled copper tubing followed by a rotameter. The rotameter was used to set an approximate flow rate during start up while the Brooks flowmeter was used to measure flow rate during data collection.

All major cryogenic components- namely the tanks, dewars and transfer hoses are connected to the unistrut structural framework. Extensions to the existing unistrut frame, as indicated in Fig. 10, was needed to secure all cryogenic components. This framework was used to build a safety enclosure around the cryogenic tanks to ensure that there is no risk of toppling of these tanks. Further safety considerations are provided in appendix A.

Table 2. List of instrumentation and equipment for the facility shown in Fig. 9

Instrumentation/ Equipment	**Manufacturer**	**Model**	**No.**	**Range**
Cryogenic tank	Chart Industries	Cryocyl, 10648610	1	80 liters capacity @ max P of 15 bar
Cryogenic tank (rental)	Airgas		1	160 liters @ ~1.5 bar
Vacuum insulated cryogenic transfer hose	Chart Industries	MVE VJ Flex Hose	2	In 2 and 5 feet length and ID of 3/8”
Cryogenic transfer hose and phase separator	Airgas	TBD	1	
MVE RD6	Airgas	13982293	2	Stainless Steel with 6 liters capacity

Square Heater	Minco	HK5417R36.1L12A	1	400 W, 120 VAC, -200 to 200 °C
Rope Heater	Minco	HK5203R23.3L12A	1	618 W, 120 VAC, -200 to 200 °C
Variable Voltage Output Transformers (Variac)	Newark	66F3591	2	Power Rating:1.3kV
LN2 Valve	Hoke	4212F4Y	1	-196 °C to 316 °C
N2 Detector	Airgas		1	
Normally open solenoid valve	TBD		1	
Normally closed solenoid valve	TBD		1	
Rotameter	Omega	TBD	1	
PID controller	Omega	TBD	1	
Relay for PID controller	Omega	TBD	1	
Absolute Pressure Transducer	Validyne	P2 – 100	1	0 – 100 psia
Differential Pressure	Validyne	DP15 – 46	1	0.08 – 50 psi

Gauge				
Demodulator for above	Validyne	CD15 (A-1-A-1)	1	
N2 Mass Flow Meter	Brooks	SLA5863	1	4 – 200 slpm
CompactDAQ chassis (4 slots)	National Instruments	cDAQ-9174	1	Chassis
16 channel isothermal TC module 24 bit	National Instruments	NI 9214	1	24 bit, typical error less than 1 ^{o}C at -200 ^{o}C; sensitivity 0.01 ^{o}C
T-type Thermocouples	Omega	TJ36-CPSS-116U-3	8	-250 to 350 °C
T-type Thermocouples	Omega	TJ36-CPSS-116U-2	3	-250 to 350 °C

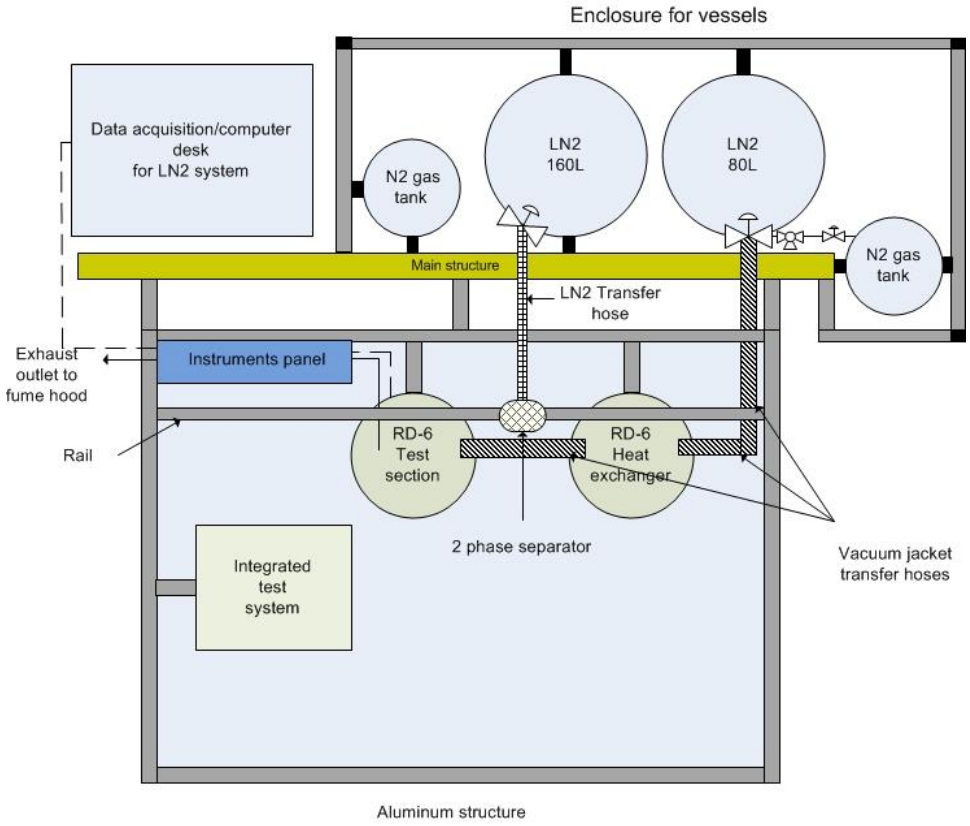

Figure 10. View of the test facility from a top view, indicating the unistrut framework and main components. Also shown is the location of the integrated test facility, which will be using the gaseous nitrogen from the compressed bottles.

2.4. TEST FACILITY

Based on the design and safety considerations detailed in the prior sections, a test section and test facility was assembled. Fig.11 shows the installed enclosure that housed the cylinder vessels while Fig.12 shows the metal shroud that housed the testing facility. Fig.13 shows the components of the facility that are located within the metal shroud.

Figure 11. Installed enclosure

Figure 12. Sheet metal shroud enclosing the test facility. The facility is located under the hood shown in the picture.

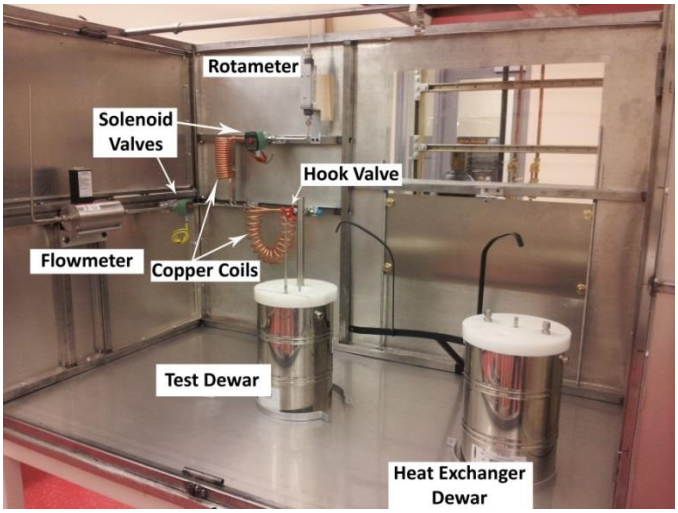

Figure 13. Test dewars and equipment inside the metal shroud

Fig. 14a shows an assembled view of the fluxmeter with thermocouples in placed and insulated with Teflon. Fig. 14b shows the assembled test section with guard heater used to ensure 1-D conduction through the fluxmeter.

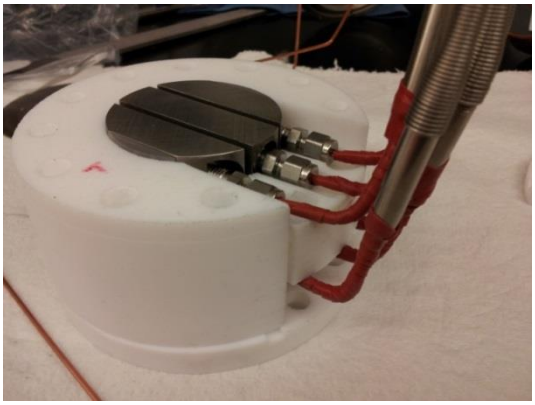

(a) Wrapping the TCs with stretch tape

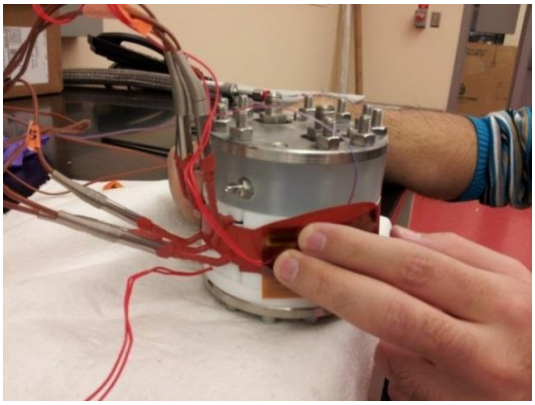

(b) Using a guard heater around Teflon insulation

Figure 14. Pictures of the test section showing (a) fluxmeter with insulation and (b) assembled with guard heaters

2.5 DEBUGGING EXPERIMENTS

Preliminary experiments to characterize the heat balance were performed in the facility described in the previous sections. The goal of these tests was to determine whether the fluxmeter could be used to obtain accurate estimates of the heat flux, as well as to identify the heat loss paths in the test section. As seen in Eq. 10, an estimate of heat flux through the fluxmeter requires that the 1-D assumption is satisfied as well as that the thermal conductivity of the fluxmeter be known precisely. The first condition was ensured by use of the insulation and guard heating. It was assumed initially that the material of the fluxmeter was pure titanium whose thermal conductivity was known. Table 3 shows results for three mass flow rates and a fixed heater input electrical power of $19.5\,W$. The guard heaters were activated during all these tests. As seen from the electrical heat input and absorbed heat by the fluid, significant error in heat rate estimation occurs, especially at low mass flow rates (and hence low heat rates) of $0.11\ g/s$. The heat rate determined from the fluxmeter with an originally assumed value of $k = 21 W/mK$ (see last column of Table 3) significantly over-predicted the electrical input heat flux. Hence, the material of construction of the fluxmeter was in question.

Table 3. Values from preliminary experiments to estimate heat flux using the Titanium fluxmeter

$\dot{m}(g/s)$	Heater power (W)	Q_absorbed (W)	Q measured by Heat flux meter (W) when k_{Ti} = 7 (W/mK)	Q measured by Heat flux meter (W) when k_{Ti} = 21 (W/mK)
0.11	19.5	6.66	11.8	35.59
0.23		12.35	14.69	44.46
0.35		14.21	15.61	48.12

A Laser Flash method was used to measure the thermal diffusivity (α) of a sample from the same material used in the fluxmeter. Since the density (ρ) and specific heat (c_p) of titanium are almost the same for different titanium grades, hence, thermal conductivity can be calculated as,

$$k = \alpha \rho c_p \tag{11}$$

Based on the restrictions of instrument, measurements were performed from the lowest possible temperature, 40℃ to about 200℃ $(313 - 473\ K)$. The variation of thermal conductivity of titanium sample with temperature is shown in Fig. 15.

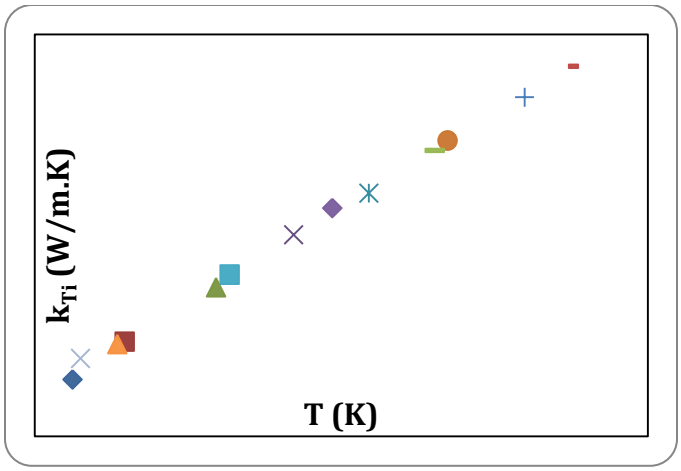

Figure 15. Variation of thermal conductivity of titanium sample with temperature

The curve fit equation in Fig. 15 has been used in later data analysis to reduce uncertainty in the heat flux measurement using the fluxmeter. From the results in Fig. 15, it is clear that the thermal conductivity of the fluxmeter was 3 times lower than what was initially assumed based on the information of the grade of Ti used. Table 3 shows a revised estimation of the heat flux using the fluxmeter based on the revised thermal conductivity of 7 W/mK from Fig. 15. The design flow rates for the experiments were between 0.5 g/s and 2 g/s. From Table 3, it can be seen that the difference between the fluxmeter estimated heat rate is within 10 percent of that based on heat absorbed by the fluid for a mass flow rate of 0.35 g/min.

While the fluxmeter conductivity determination has helped tremendously with prediction of accurate heat rates, the thermal conductivity data could only be obtained in a range of 313 – 473 K. Hence, there is uncertainty in extrapolating the conductivity values down to 80 – 130 K range which is the anticipated temperatures in the fluxmeter with liquid nitrogen flow. There is some data in literature, albeit for a different grade of Ti, which shows there is a non-linear drop in thermal conductivity at such low

temperatures. Thus, a decision was made to remove the fluxmeter and use the net electrical heat input as a measure of the heat rate to the fluid. The net heat input was determined upon accounting for heat losses in a calibration experiment as discussed in the next section.

The initial design of the flow loop following changes made through the process of debugging that lead to the final flow loop used for the data presented are detailed herein. The vacuum hose connected to the heat exchange and test section dewars were found to amass heat through the insulation, which caused the fluid temperature to rises to about $84.5K$ at the heat sink inlet plenum. In order to recuperate the degree loss of subcooling, a second stage of subcooling was added to the system to compensate that temperature increase. This subcooling is realized by utilizing a .25" copper tube coiled around the test section enclosure (see Fig. 16) that is immersed within the test section dewar. The inlet temperature of about $80K$ was achieved by this method at the inlet plenum.

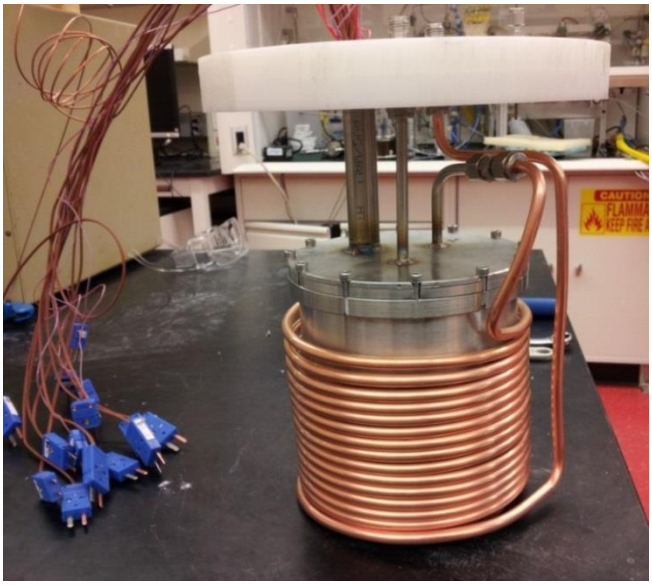

Figure 16. Copper coil used as second stage subcooling

Even after the temperature entering test section was corrected by adding the second stage of subcooling, the issue of pressure fluctuation at the inlet of test section still persisted. Liquid nitrogen is a very volatile fluid and small heat loss into the fluidic lines could cause phase change and local subcooled boiling. Hence, the lines have to be as short as possible and fully insulated. Based on the flow loop design described above, there are two stages of subcooling before entrance of the flow into the test section. First stage was in the heat exchanger dewar and second through a copper coil immersed into the test dewar. It was decided to exclude the first heat exchanger dewar from the flow loop and connect the $80L$ cryo-cyl directly to the test dewar using $5ft$ vacuum jacket insulated transfer hose. Thus, the fluidic lines would be much shorter and subcooling would only take place in the test dewar. The result showed dramatic reduction on fluctuations and stable flow conditions at the inlet.

Figure 17 shows the time series of absolute pressure at the inlet of test section for two flow rates with and without the heat exchanger dewar in the flow loop. With the heat exchange dewar in place, pressure oscillations as large as $110\ kPa$ were seen at a flow rate of $2.33\ g/$s. With the elimination of the dewar, the fluctuations were non-existent at this flow rate and minimal at the higher flow rate of $3.8\ g/s$. For flow rates less than $2\ g/s$, instabilities in pressure and temperature existed downstream of the microchannel, caused most likely due to the phase-change process downstream prior to entering the mass flow meter. Hence, data collection was limited to the $2-4\ g/s$ range of flow rates.

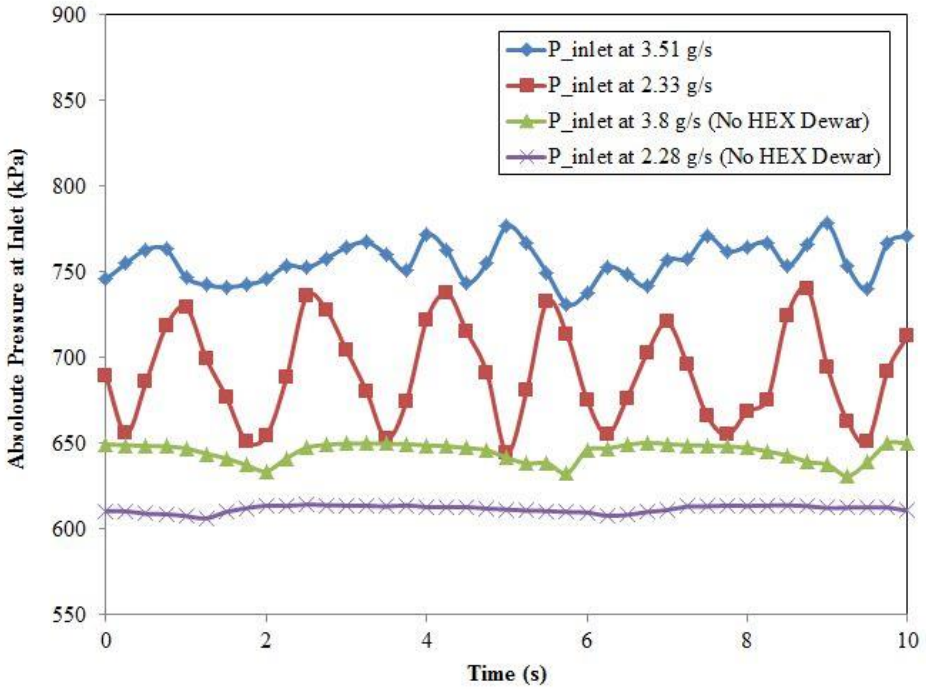

Figure 17. Time series of inlet absolute pressure for cases of with and without the Heat exchanger dewar

The mass flow rate of LN_2 through the heat sink is measured using a high-accuracy gas flowmeter that is located at the exit of the test facility. The LN_2 flow needs to be heated past the heat sink, vaporized, and heated to a temperature of ~20 ℃ prior to entering the flowmeter. To prevent of damage to the flowmeter should colder gas or LN_2 enter the flowmeter, it was important to perform a series of tests to evaluate whether complete LN_2 evaporated inside the line prior to the flowmeter.

The initial system had a series of electrical rope heaters wrapped around the line prior to the flowmeter in order to vaporize and preheat the gas. Debugging tests were performed with liquid nitrogen flowing through the test section and without applying heat to the test section. This provided the worst-case of heating that needed to be provided by

the rope heaters. These tests showed that the rope heater power had to be substantially high which lead to burnout. The upshot of experiments was the addition of a temperature controlled heater bath to the system. It consists of a hot bath filled by Paratherm LR oil and a copper coiled tube in overall length of $40\ feet$ immersed in the hot bath. With the bath temperature adjusted to $50\ ℃$, it was found sufficient to vaporize LN_2 and increase the temperature of the cold gas to $20℃$, even for the highest flow rate. Fig. 18 shows a picture of the hot bath during testing. The inlet tubing was covered with frost while the exit tubing was frost-free.

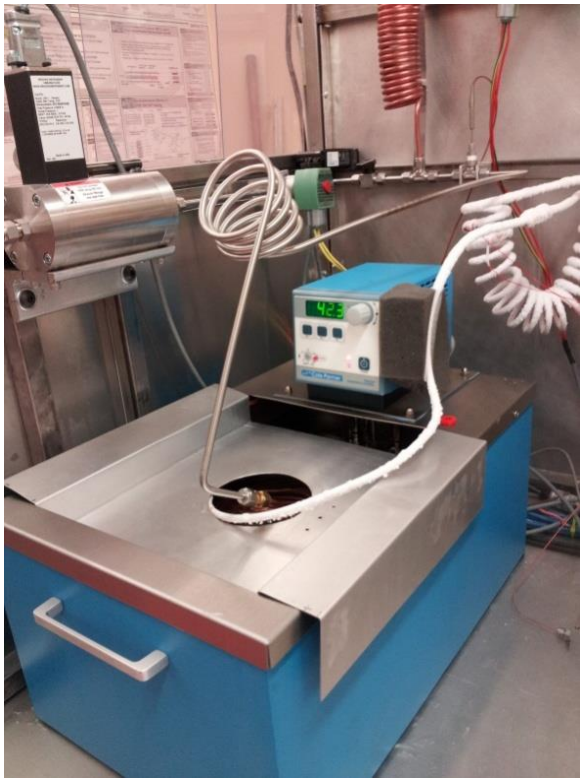

Figure 18. Heater bath connected prior to the mass flow meter

2.6 FINAL TEST SECTION DESIGN

The final design of the test section was different from the original in two key features. The titanium fluxmeter and pressure ports on the header were removed. Due to the uncertainty of extrapolating the thermal conductivity data for the fluxmeter at the range of working temperature discussed, the fluxmeter was removed and the net electrical power was used as an estimate of the heat input to the microchannel heat sink. The net power was determined using the measured voltage and current and subtracting the heat losses through a calibration experiment. Pressure readings at the inlet plenum were unstable with the original header design shown in Fig. 17; hence the pressure ports were also relocated outside the header and test assembly.

Figure 19 shows an exploded view of the assembly of the final test section design. A thick film serpentine heater (Minco Inc.) of 50.8 x 50.8mm dimensions was used to provide the desired heat flux to the heat sink. The heater was powered using a variable DC power supply. The heater was placed between two circular aluminum disks each of diameter 70mm and 1.5mm in height. Six thermocouples (see Fig. 20 for locations) were sandwiched between the microchannel heat sink and the upper plate. The bottom disk, located between the heater and a thick PVC insulating block, prevented damage to the heater from the compression force of two stainless steel inserts shown in Fig. 19. The inserts helped to maintain a constant sealing pressure on the o-rings during the thermal stresses caused by different contraction rates of materials in the test section during the cryogenic chill down. The test section was assembled together using twelve stainless steel bolts and nuts. Cryo-gel insulation (Aspen Aerogels®) was used to wrap the test section before it was placed inside a stainless steel enclosure. The enclosure was

in turn submerged within a 10 $liter$ dewar filled with liquid nitrogen. Surrounding the test section in such an environment minimized the parasitic heat gain from the surroundings.

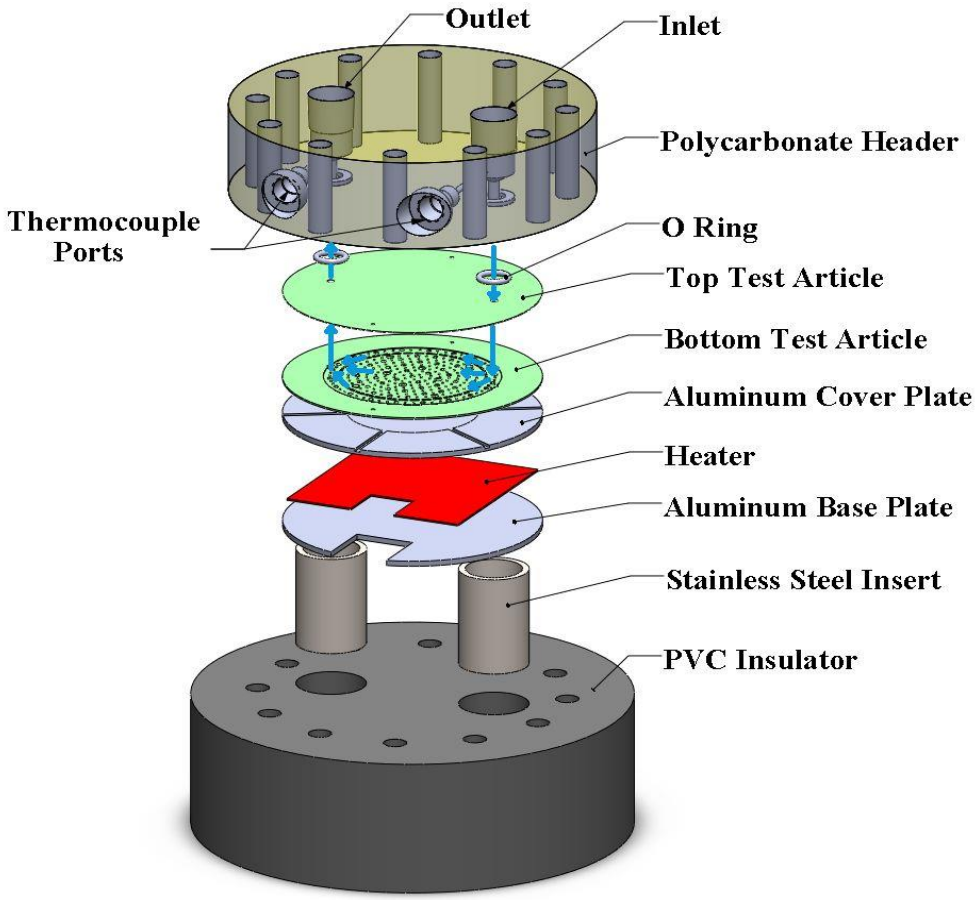

Figure 19. Assembly view of the test section

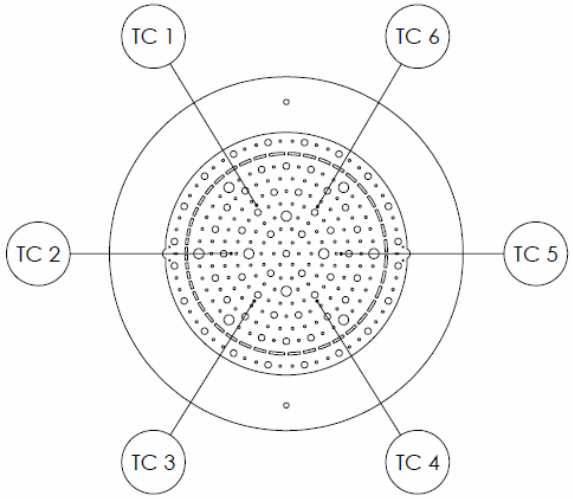

Figure 20. Locations of the thermocouples

2.7 FINAL FLOW FACILITY

The original flow facility went through several iterative changes based on feedback from the preliminary data gathered. The changes made were primarily to eliminate pressure fluctuation upstream of the heat sink, and ensure complete vaporization of the liquid nitrogen in the downstream of the heat sink before it entered the flowmeter. Fig. 21 shows the updated schematic of the experimental facility following debugging. In summary, the modifications resulted in placement of the subcooling heat exchanger coil upstream of the heat sink in the same dewar as the test section enclosure. A hot oil bath was used in place of rope heaters downstream of the heat sink to ensure complete vaporization of LN_2 prior to entering the gas flowmeter.

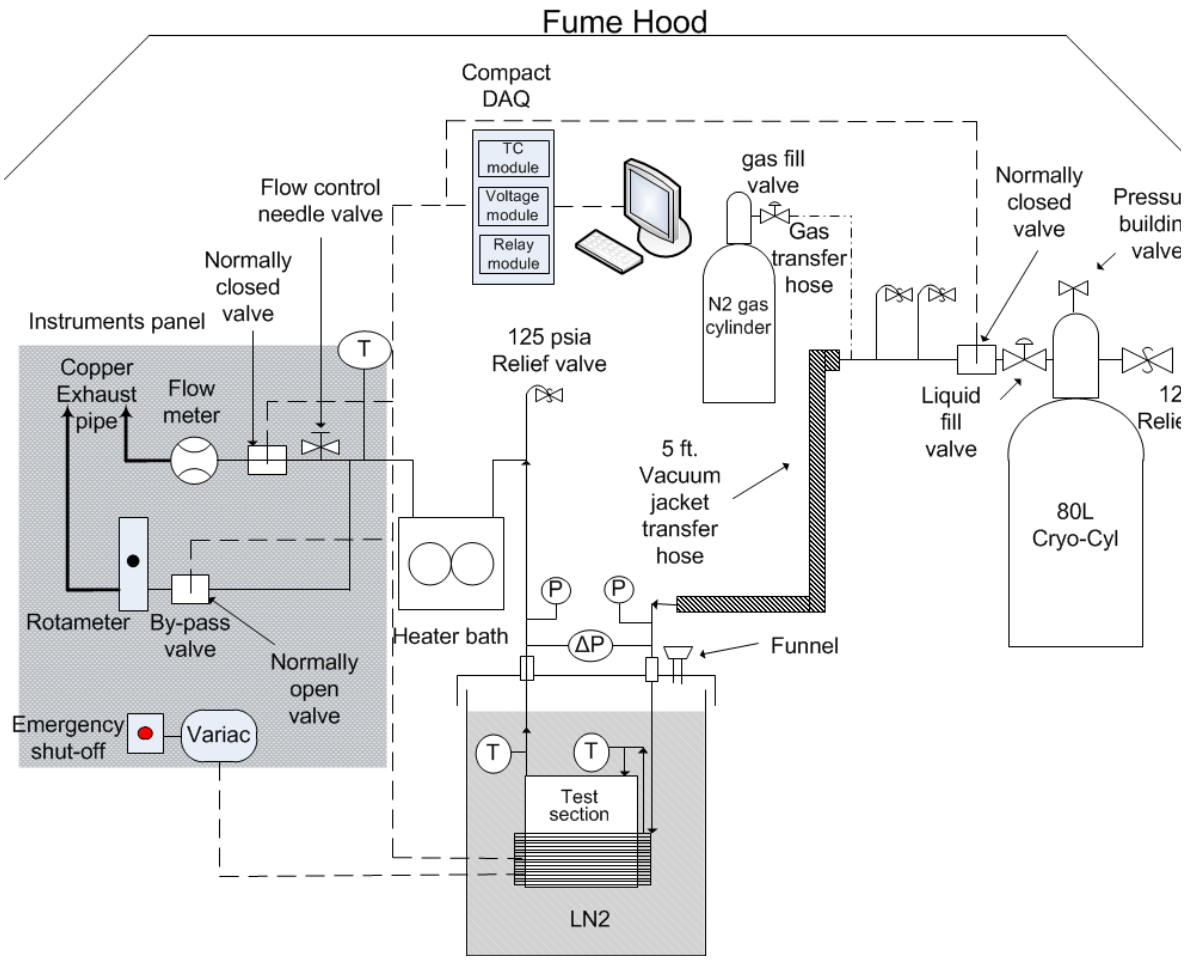

Figure 21. Final liquid nitrogen flow facility schematic

2.8. EXPERIMENTAL PROCEDURES

The experimental procedures were broken down into four parts: (a) start up, (b) continuous operation, (c) shutdown and (d) emergency shutdown. The procedures also included safety checks that were performed during an experimental run. Figures 22 through 26 present flow charts of the procedures; in addition, a bulleted list is also provided with some additional details.

2.8.1 STARTUP PROCEDURE

There were two steps to the start-up procedure. The first involved reconnecting and reassembling hardware and instrumentation that might have been previously used in a companion integrated testing by another student; the second involved start up procedures prior to steady state data collection.

Startup procedures Step I: *Re-assembling hardware and instrumentation for separate effects tests*

Prior to handling the equipment in the facility, face shield, apron, and cryo-gloves were worn for protection. The oxygen meter (Industrial Scientific) located in the walk-in hood where the facility was located was checked to ensure the O_2 level in the lab was greater than 19.8%. The hood was turned-on to vent vaporized LN_2 during operation. Valves for the $80L$ and $160L$ cryogenic cylinders were inspected for closure. The cryo-cylinders were also tugged at to make sure it was secured to the unistrut frame. The transfer hoses were examined for securely mounted to the unistrut support and unattached to the cryo- cylinders. Pressure and level of LN_2 for both cryo-cylinder were inspected by the pressure gauges and float indicators for safe operating range $(< 125psig)$ and sufficient $LN_2$for testing ($> 50\%$ for both vessels), respectively. The pressure regulator was adjusted to set the desire operating pressure in the $80L$ cryo-cylinder. All system was examined to make sure it was powered down.

The cap of the test section dewar was removed to check for complete evaporation of LN_2. The test section was then assembled and leak tested with compressed air while submerging in water. Once leak testing was satisfied, the test section was insulated then placed inside its housing (stainless steel can), then connected and mount inside the dewar.

The cap of the test section dewar was assembled back on and was connected to the transfer hose. Differential pressure lines were connected. Thermocouple sub-miniature connectors coming out of the dewar from the test section were connected to the data acquisition board via male and female connectors. Thermocouples from other locations in the test facility were connected to the data acquisition board. Visual inspection was made to make sure all fluidic lines from the start of the dewar to the exit of the test facility were connected. Both solenoid valves were closed using LabVIEW commands. The flow loop was leak tested to $\sim 100 psig$ using compressed air. Once leak testing of the flow loop was satisfied, the airline was replaced with the transfer hose connected to the $80L$ cryo-cylinder.

Startup Procedures Step II*: Experiment start up procedure*

Electronics to the system were powered on (pressure transducer and mass flowmeter) and the heater bath temperature was set to $\sim 20℃$. LabVIEW program was tested for proper readings from all instrumentation. N_2 was run through the system to remove any condensed liquid.

The dewar was filled with LN_2 by gradually opening the valve on the $160L$ tank. Extra precautions were taken to keep shielded and distance from the dewar during the initial stage of filling. When LN_2 made contact with the dewar walls, there was rapid boiloff due to film boiling and then nucleate boiling. For this reason, filling the dewar was performed with caution.

Once the heater bath reached$\sim 20℃$, the normally closed valve was activated through LabVIEW. The valve of the $80L$ cryo-cyl was opened gradually to start flow of LN_2 through the system. The initial liquid rapidly boiled off upon entering the

fittings/tubing. Within minutes, the system chilled and liquid was flown through the heat exchanger and heat sink. Temperatures at the exit of the heat exchanger and the inlet and exit of the heat sink were monitored through LabVIEW to guide the operator (s) aware of the gaseous to liquid phase transition through the system. Once liquid in the system was verified, the system was then set for continuous operation.

Thermocouple probes affixed $3cm$ from top of the dewar were used to determine whether and when LN_2 level in the dewar was low. The LabVIEW program prompted the operator when the temperature reading of the thermocouple went above the set limit $(80K)$. The fill hose connected to the $160L$ was then turned on to fill the dewar until the temperature reading of the thermocouple drops to $\sim 78K$.

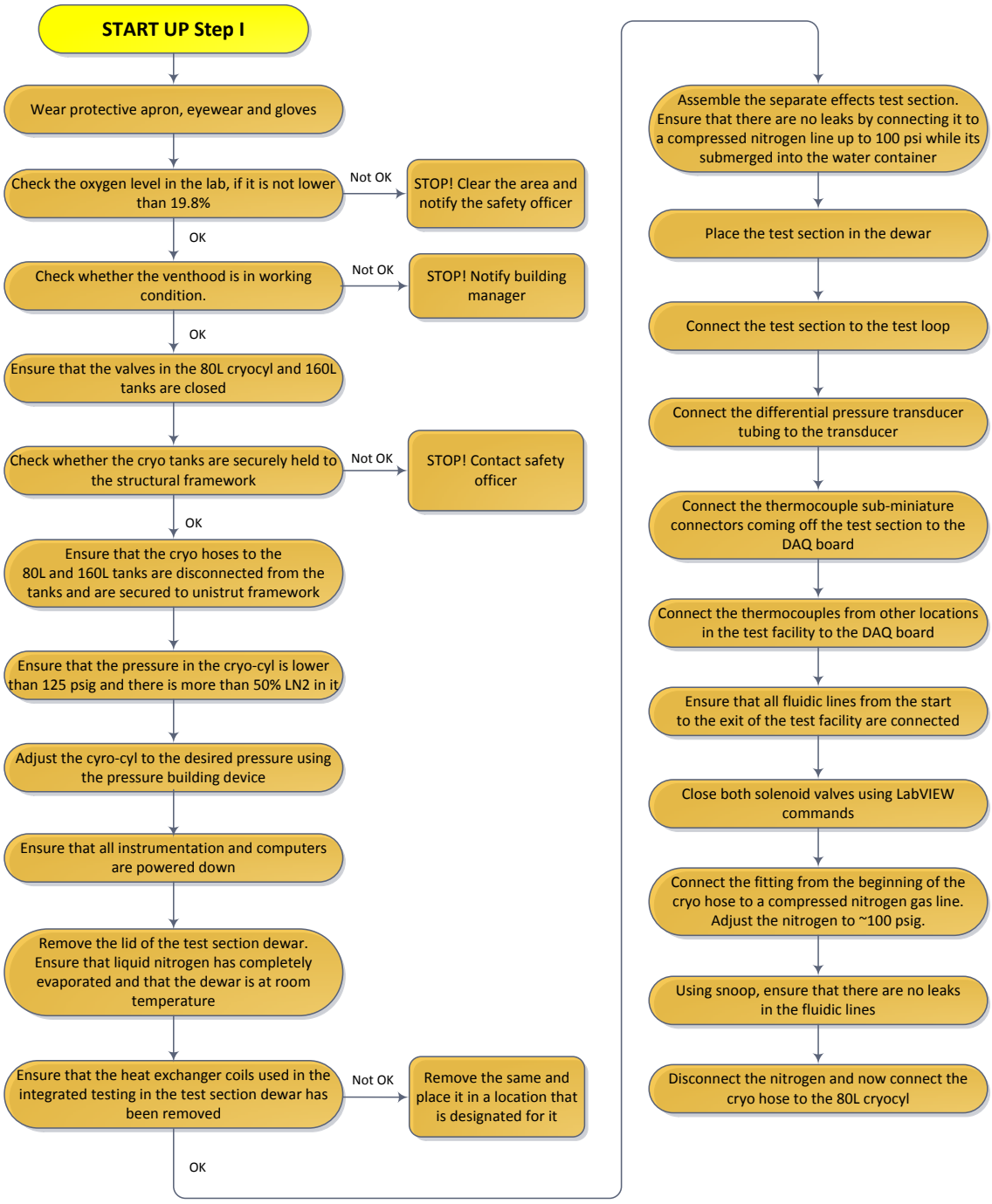

Figure 22. Startup procedure I- Re-assembling hardware and instrumentation for separate effects test

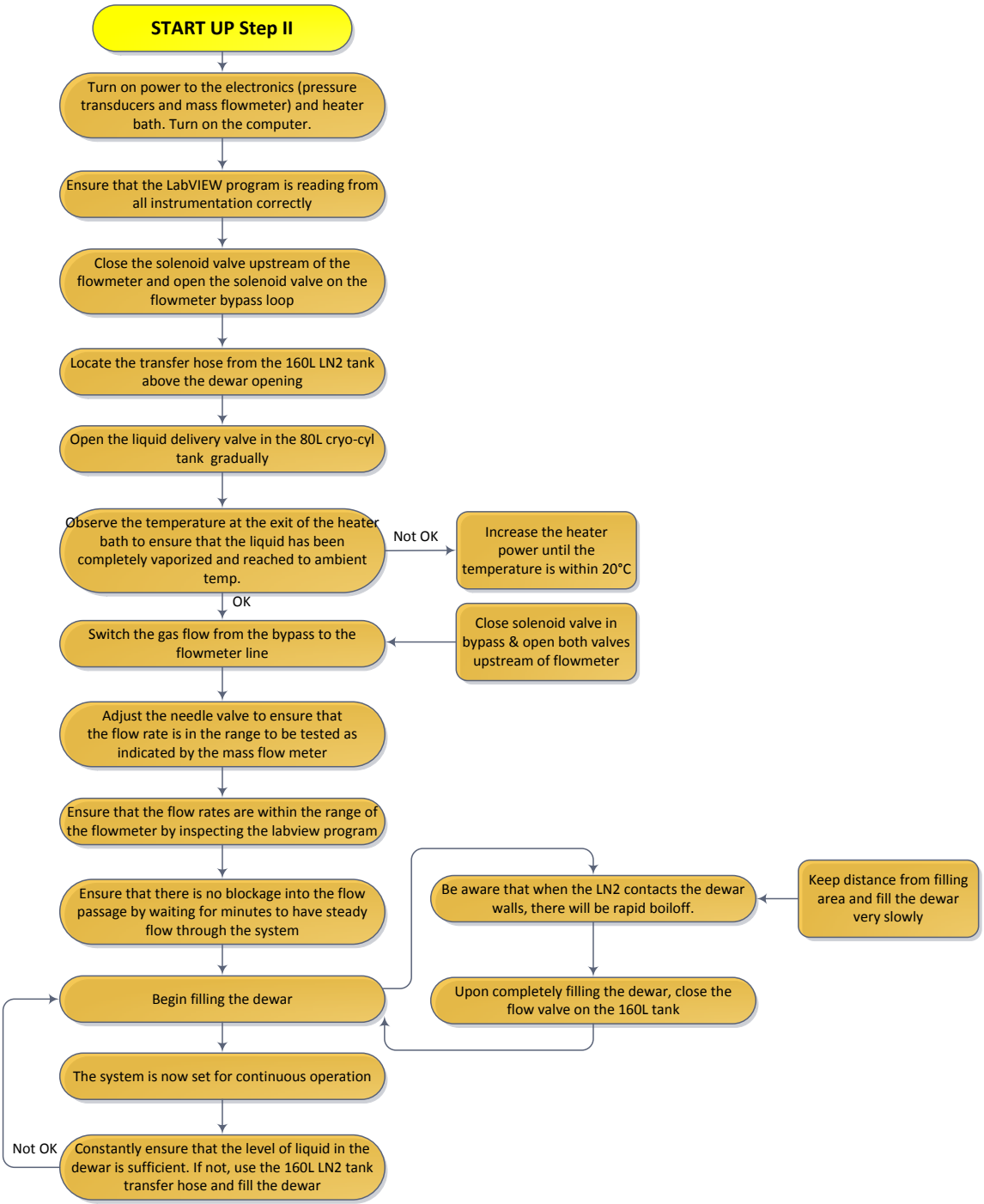

Figure 23. Startup procedure II flowchart

2.8.2 CONTINUOUS OPERATION PROCEDURE

Flow rate was adjusted using the fine-turn needle valve. The flowmeter and pressure drop outputs were monitored through LabVIEW to ensure steady flow was achieved through the system. A variac controlling the thick film heater that supplied power to the test section was turned on and adjusted to the operating input power. The surface thermocouple temperatures were monitored to ensure that their values did not exceed the saturation temperature at the recorded pressure within the heat sink. This procedure ensured that single phase flow existed throughout the heat sink. Another constraint was that the temperature difference between the inlet and outlet be less than 5°C for reduced uncertainty between heat flux recorded by the net input power and heat gain in the fluid.

The level of LN_2 in the dewar was continuously monitored and filled as needed. Heat flux, surface temperatures, and exit temperature of the fluid was monitored for steady-state. Data were recorded when steady-state was reached. Power input from the variac was reduced before the next flow rate was tested.

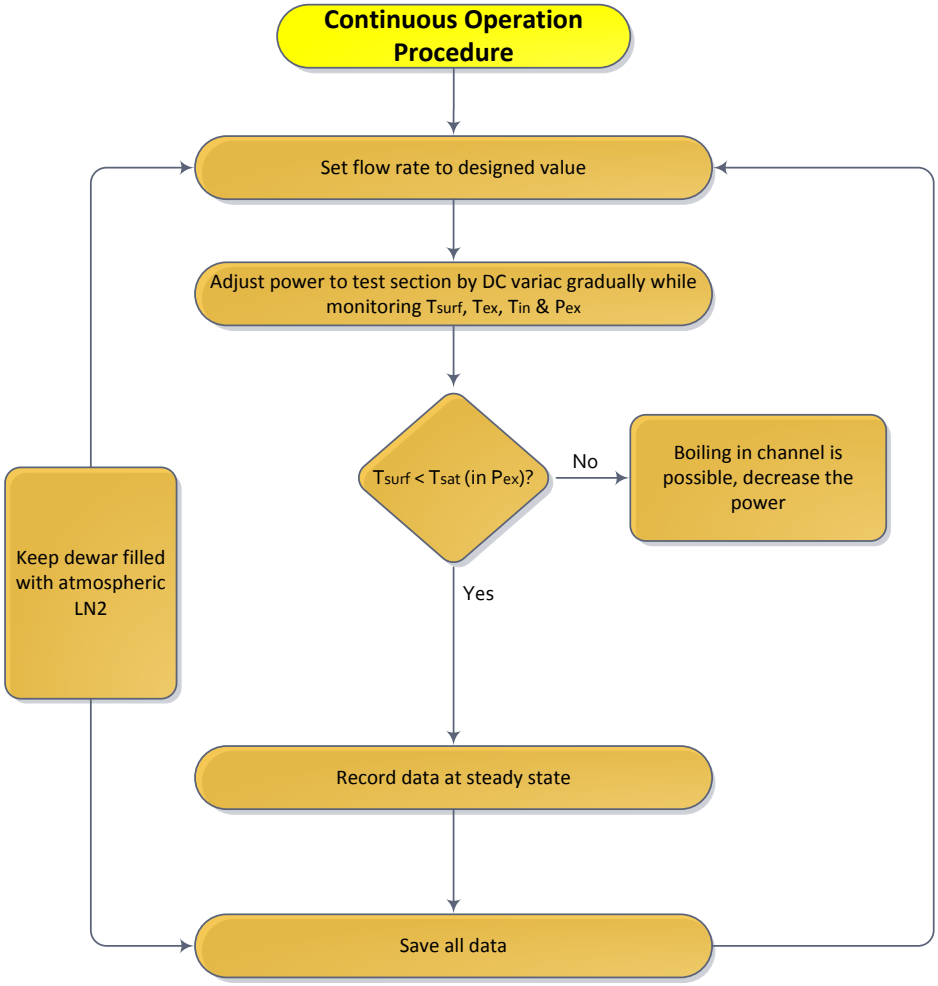

Figure 24. Continuous operation procedure flowchart

2.8.3 SHUTDOWN PROCEDURE

Power to the variac was turned off. Once the surface temperatures of the heat sink were within 2 degrees of the exit temperature, the flow valves on both cryo-cylinders were shut-off. Power to the heater bath was turned off. Once liquid nitrogen in the dewar had evaporated and the temperatures in the test section was near ambient, the fittings were disconnected to the inlet and exit of the test section dewar. The cryogenic transfer hose was kept resting securely on the frame support.

All thermocouple and pressure connections were disconnected from the test section. The test section was then removed from the dewar. After the lid was put back on the dewar, the test section was placed in a secure location. The $5\text{-}foot$ transfer hose was detached from the $80L$ cryo-cylinder and securely fixed on the frame support. Electronics and instrumentation were powered down. The transfer hose line was disconnected from the $160L$ cryo-cylinder.

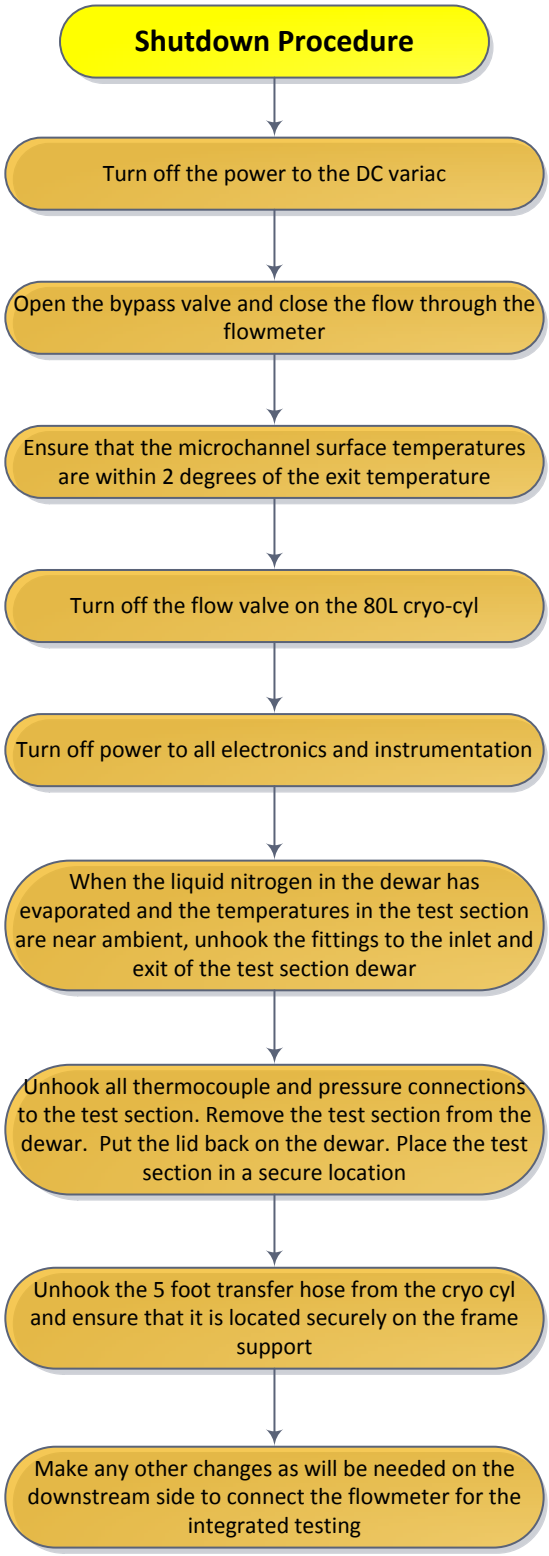

Figure 25. Shutdown procedure flowchart

2.8.4 Emergency Shutdown Procedure

The emergency procedures shown in Fig. 26 were to be followed in case of a building fire or evacuation, if the oxygen level in the room dropped below unacceptable levels, or if there was a rupture in the fluidic lines. Firstly, the valves to both the liquid N_2 tanks would be closed, if possible. One would then ensure that the fume hood fan was operating. An emergency stop switch located near the lab exit would be depressed. This would cause the heater and electronics power to turn off and the LN_2 solenoid valve to close. The operator would then exit the lab and notify the building manager and safety manager.

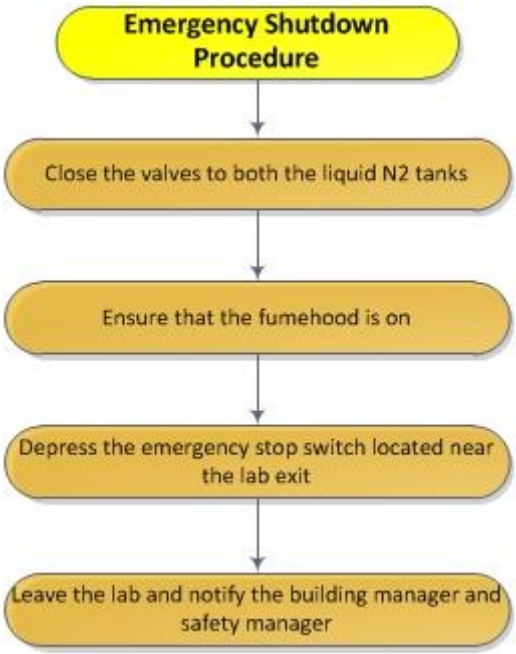

Figure 26. Emergency shutdown procedure flowchart

3. EXPERIMENTAL DATA REDUCTION AND UNCERTAINTY ANALYSIS

Chapter 3 presents analyses of experimental errors in data measured and equipment used for measurements. Equations used for determining values and correction in data, along with corrected calibration are present first, follow by uncertainty analysis of the error in equipment used.

3.1 DATA REDUCTION

The average Reynolds number, $\overline{Re}$, within the heat sink was based on an average of the Re_{local} (determined using Eq. 1) from x/D = 0.15 to 0.8. As mentioned in Section 2.2.1, the pressure drop was measured between an upstream location prior to the heat exchange coils (see Fig. 16) and the exit of the test section. In order to correct for pressure drop within the fittings and the heat exchange coils, a calibration experiment was performed. In the calibration experiment, the microchannel heat sink and the polycarbonate header shown in Fig. 21 were removed and the flow path was shunted using a small length of $6.35mm$ outer diameter tubing. Pressure drop was recorded as a function of flow rates used in the actual experiments. The pressure drop across the heat sink was then estimated by subtracting this pressure drop from the calibration experiment.

The pressure drop is represented non-dimensionally in terms of the friction factor;

$$f = \frac{\Delta p(\bar{D}_h/\bar{L}_c)}{\rho\vec{v}^2/2} \tag{4}$$

where $\bar{D}_h$ and $\vec{v}$ are based on the average hydraulic diameter and cross-sectional velocity between x/D of 0.15 and 0.8. The characteristic length, $\bar{L}_c$is determined as:

$$\bar{L}_c = \frac{\forall_{hs}}{\bar{A}_c} \tag{5}$$

where $\forall_{hs}$refers to the fluid volume within the heat sink and $\bar{A}_c$ refers to the averaged cross sectional fluid area between x/D = 0.15 and 0.8.

The area-averaged Nusselt number from experiments, $\overline{Nu}$, was determined as:

$$\overline{Nu} = \frac{\bar{h}\bar{D}_h}{k_f} \tag{6}$$

where k_f is the thermal conductivity of the fluid estimated at the average bulk fluid temperature. The area-averaged heat transfer coefficient in Eq. 11 was determined using the Newton's law of cooling based on assumption of uniform heat flux boundary condition on the bottom side of the heat sink,

$$\bar{h} = \frac{q''_{net}}{(\bar{T}_{wall} - \bar{T}_{bulk})} \tag{11}$$

where $\bar{T}_{wall}$ represents the average temperature measured by the six surface thermocouples shown in Fig. 20 and $\bar{T}_{bulk}$ represents the average between the inlet and exit bulk fluid temperatures. In Eq. 11, the net heat flux was estimated based on the electrical heat input power, less the heat losses, and the heat sink surface area,

$$q''_{net} = \frac{Q_{net}}{A} = \frac{Q_{elec} - Q_{loss}}{A} \tag{12}$$

The heat loss, Q_{loss}, was estimated based on a separate calibration experiment. In this experiment, the flow lines were connected to a vacuum pump and the test section and heat exchange coil were immersed in liquid nitrogen as in the actual experiment. Steady state temperatures were recorded for a range of input power to the test section to obtain a heat loss estimate as a function of surface temperature. Such a calibration curve is shown in Fig. 27, wherein the average of all six thermocouples is used to determine the heat sink wall temperature. It can be seen that the trend of heat loss with temperature is nearly linear, indicating heat loss via conduction through the test section assembly. It is also seen that the heat loss values are quite small ($< 4\%$ of input heat flux at worst).

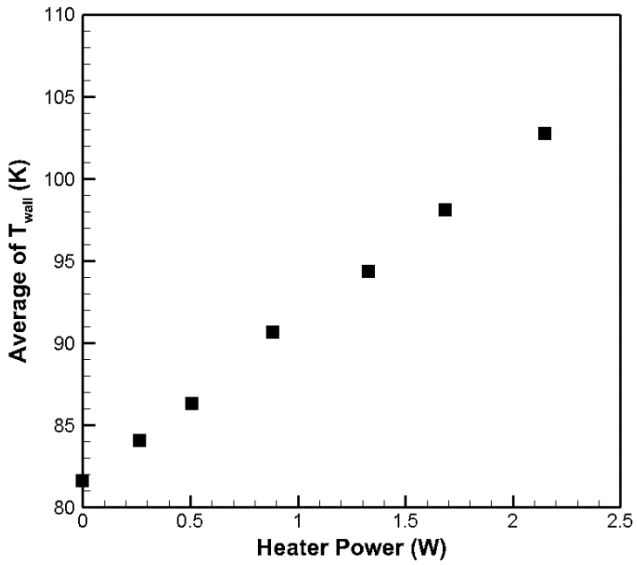

Figure 27. Calibration curve for Q_{loss}

3.2 UNCERTAINTY ANALYSIS

Thermocouples, absolute and differential pressure transducers were calibrated using a NIST-traceable hand held calibrator (Omega, PCL-1B) as a standard. The calibration error included errors associated with the calibrator, the calibration precision error and the curve fit error. The gas flow meter was factory calibrated.

The errors in measured and determined variables are listed in Table 4. The Kline and McKlintock error propagation method [19] was used to determine uncertainties in the calculated parameters based on the bias and precision errors of the measured variables. Uncertainties in measured parameters were obtained by combining the measurement precision calibration errors in a root-sum-square manner. Engineering Equation Solver (EES, Fchart Inc.) was used to perform the propagation of errors. Maximum uncertainty in measured variables was propagated into the dependent variables using the appropriate equations in this section.

Table 4. Representative measurement uncertainty estimate

Variable	Maximum Uncertainty ($\pm$)
Volumetric flow rate	$\pm 0.12\ slpm$ (0.1%)
Voltage supplied by DC power supply	$\pm 0.2V$ (0.6%)
Average fluid and surface temperature, T	$\pm 0.3K$ (0.35%)
Heat flux, $q^{"}$	$\pm 300\ W/m^2$ (1.7%)
Absolute Pressure	$\pm 1\ kPa$ (0.16%)
Pressure drop, Δp	$\pm 0.5\ kPa$ (0.8%)
Average Reynolds number, $\overline{Re}$	± 20 (2.3%)
Friction factor, f	± 0.2 (4.2%)
Average heat transfer coefficient, $\bar{h}$	$\pm 120\ W/m^2 \cdot K$ (4.4%)
Average Nusselt number, $\overline{Nu}$	± 0.5 (5.1%)

4. COMPUTATIONAL FLUID DYNAMICS MODEL

This chapter describes the three dimensional CFD simulation of the fluid flow and heat transfer performed in ANSYS (Version 14.5). Details of the mesh generation for the fluid volume of the heat sink in ANSYS Workbench to set up for the computational fluid flow model to be solved in ANSYS Fluent, governing equations and assumptions used, scheme and convergence limits selected are presented.

4.1 MESH GENERATION

The fluid volume of the heat sink was used as the geometry for the computational model. The geometry was generated in SolidWorks then imported into ANSYS Workbench for meshing. To save computing time, symmetry along the inlet and exit was exploited and only one half of the heat sink was modeled and used for simulations.

The mesh volume was generated by controlling parameter settings for global and local control in ANSYS Workbench. Boundary layer at the walls was modeled for the no slip condition imposed. The physics preference solver was defined in global settings along with parameters to control the fineness of the mesh, elements quality, and inflation layer for the top and bottom walls surface. Local control was added to specify the specific meshing method used, chosen for the built in function that allows control over the number of layers and inflation bias between the top and bottom walls of the geometry.

Within global control settings, parameters for the mesh solver, mesh fineness, elements quality, inflation for the top and bottom surface was defined. Mechanical physics preference was selected as the solver for the application. Mesh fineness was controlled under relevance settings that ranges -100 to $+100$, where the minimum end

of the scale produces a course mesh and improves as the number of relevance increases up to the maximum which dictates the finest mesh the solver is able to produce relative to parameter defined in other settings. Further details for this setting are provided in the grid independence study, section 4.3. Elements quality was controlled under smoothing, transition, and span angle parameters. A high setting for smoothing was chosen from choices of low, medium, and high, for more iteration steps to improve element quality by rearranging nodes relative to other nodes and elements. Slow transition was selected to control elements growth rate relative to each other to produce smoother transitions as contrast to a fast setting that would results in greater abruption in transitions. Span angle center refines elements at curvature where mesh in curved regions gets subdivide until each elements span the angle within the range defined for coarse (60° - 90°), medium (24° - 75°), and fine (12° - 36°) settings. For this control, a fine setting was selected. The no slip condition imposed at the pin fin walls was modeled with boundary layer for the top and bottom walls surface under inflation grouping. Within this grouping, inflation was chosen to inflate outwardly from the pin fin walls with parameters defined for the first layer thickness, maximum number of layers and growth rate. The first layer thickness, or element height nearest to the pin fin's walls, was specified as $.1\mu m$. The maximum number of inflation layers was set to 15. As the name indicates, this parameter controls the maximum number of inflation layers, counting from the first minimum to the last maximum layer's thickness. Growth rate of 1.2 was defined to control the gradual increases of each layer, starting from the first initial layer thickness defined at the pin fin's walls. All remain settings in global control were left as default. Fig. 28 shows a

detailed topview of the mesh generated from parameters controlled in global settings for a mesh size of 3 million cells.

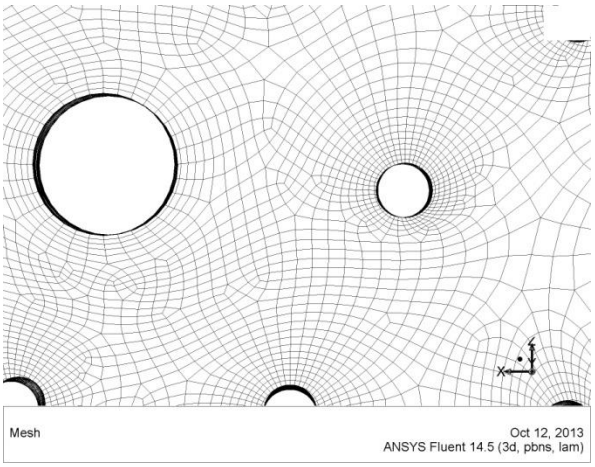

Figure 28. Detailed top view of the mesh generated from global control parameters for the case of 3 million cells

Local meshing control defined parameter in sweep method settings, used to with pure hexahedral elements to model the boundary layers between the top and bottom walls. Within parameter settings for this method, the number of sweep division and bias type was defined. The number of sweep division controls the number of cell layers that were meshed between the top and bottom walls. For the case of a mesh with 3 million cells presented, 42 division layers were specified. More on selected parameters for this setting is elaborated in grid independence study in section 4.3. Sweep bias type was chosen to inflate from the boundary walls inwardly towards the mid-plane that lies in between them. It was noted that parameters defined in local control supercedes those defined in global control, which means local meshing is a hard control and gets executed

with priority over global meshing. Fig. 29. shows a front view of the symmetry plane of the boundary layers mesh generated from parameter defined under the local meshing control settings with 42 division layers along the y-axis for a mesh size of 3 million cells.

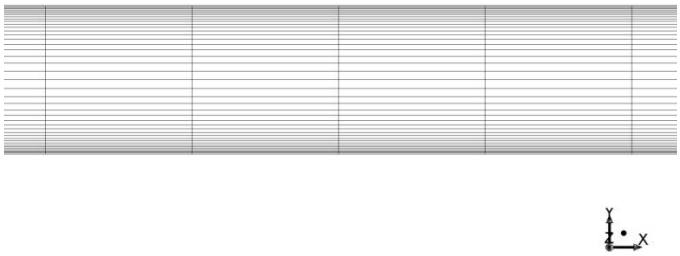

Figure 29. Front view at symmetry plane of the mesh generated from defining the gradient bias at the boundary walls for mesh of 3million cells

Fig. 30 provides an isometric view of the mesh generated for the fluid volume of the heat sink from combined parameter defined in global and local settings for the case of 3 million cells.

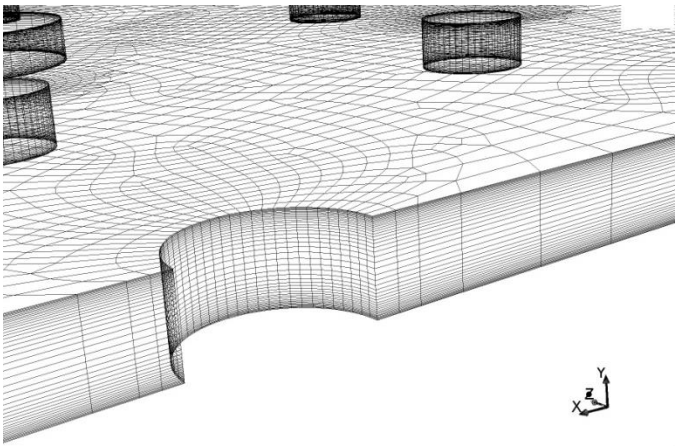

Figure 30. Isometric view of the mesh of the fluid volume of the heat sink at symmetry plane for the case of 3 million cells

Mesh quality was measured by the skewness of element's volume, for a range from 0-1, where 0 skewness is best match the shape of the element and 1 is distorted. Although all hexahedral elements volume was specified to be meshed, some portion of the model was meshed as wedges due to the complexity of the geometry. Fig. 31 shows the skewness distribution for both types of element in percent volume for the model meshed with 3 million cells. Though wedge elements were plotted in Fig. 31, it's not distinguishable due smaller percentage of its present for the entire mesh. Skewness ranged from a minimum of $1.36e$-3 to a maximum of 0.86, with an average of 0.19, and a standard deviation of 0.12.

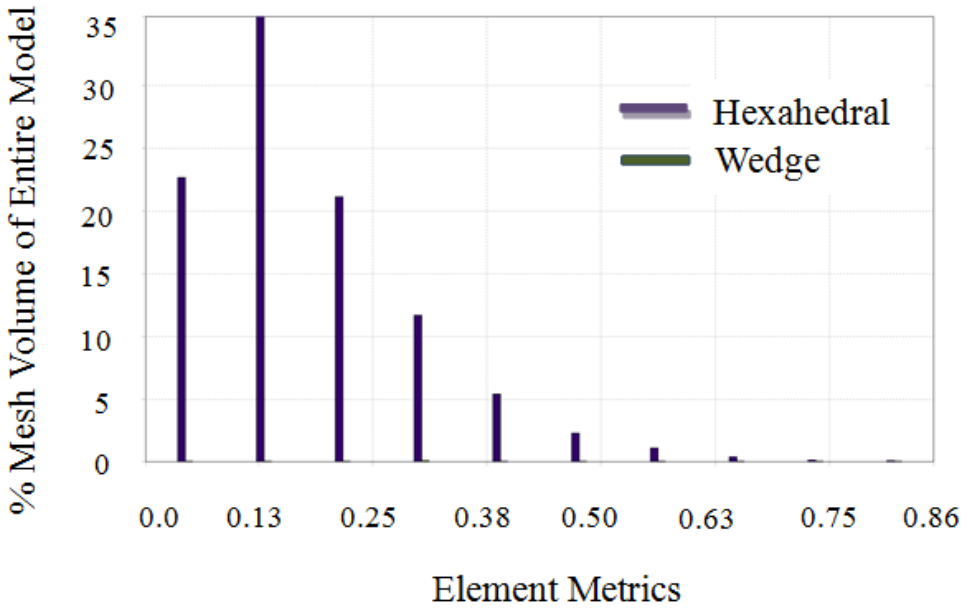

Figure 31. Skewness distribution in percent volume for the mesh of 3 million cells

4.2 GOVERNING EQUATIONS AND ASSUMPTIONS

The steady-state, incompressible, laminar governing mass, momentum and energy equations were solved for user-specified initial and boundary conditions in ANSYS Fluent. Fluid thermophysical properties were kept constant and evaluated at the experimentally measured $\bar{T}_{bulk}$. Specific properties used in the experiment for a tested flow rate was defined in Fluent. Table 5 provides the values used for flow rate of $3 g/s$. A no slip velocity boundary condition was prescribed at the pins and surface walls. A fixed velocity condition was provided at the inlet while an outflow condition was prescribed at the exit. For the energy equation, a constant heat flux boundary condition was prescribed at the bottom wall of the heat sink, while the top wall was kept adiabatic. The net heat flux from the experiment was applied at the bottom wall. The solution was initialized with the inlet fluid velocity and temperature.

Table 5. LN_2 properties used for the computational model

Property	Value
Density	793.8 (kg/m^3)
Specific Heat	2051 $(J/kg \cdot K)$
Thermal Conductivity	0.1395 $W/m \cdot K$
Viscosity	1446 x 10 $-$ 07 $kg/m \cdot s$

4.3 COMPUTATIONAL SCHEME, CONVERGENCE AND GRID INDEPENDENCE

Pressure-velocity coupling was achieved by SIMPLE algorithm and the energy and momentum equations were discretized using a second order upwind scheme [20]. Convergence criteria were specified as residuals less than 10^{-5} for the energy equation and 10^{-4} for all others.

A grid independence study was performed with mesh size of 0.5, 1, 2, and 3 million cells. Changes between the four meshes were refinement of elements on the surface of each layer and the number of layers defined perpendicular to the symmetry plane. Change from mesh size of 0.5 to 1 million cells was refinement of surface elements while the number of layers kept constant at 22 for both meshes. Changes between mesh size of 1, and 2, and 3 million cells were the number of layers between the top and bottom walls of the geometry while the surface elements were kept approximately constant due to limitation in cell refinement control. With maximum relevance set for cell fineness (+100), it was found that only about 60 thousand cells was meshed per division layer for the surface. In order to increase the number of cells, the number of layers along the y-axis shown in Fig. 33 was increased. For mesh size of 1, 2, and 3 million cells, the number of layers was increased from 22 to 28, then to 42, respectively, while all other parameter settings were kept the same for the three cases. Top views of the meshes are shown in Fig. 32 for all four cases. Changes from mesh size of 0.5 million cells in Fig. 32a to 1 million cells in Fig. 32b are noticeably significant with finer elements and greater number of inflation layers developed. Differences in the top surface elements for mesh between 1 million cells in Fig. 32b to 2 million cells in Fig. 32c were minute, and no observable differences were detected between mesh shown

in Fig. 32c for 2 million cells and Fig. 32d for 3 million cells. Fig. 33 shows the major differences between mesh size from 1, 2, and 3 million cells with increased in number of layers along the y-axis from the front view of the symmetry plane. Mesh size of 0.5 million cells has the same number of layers as 1 million cells mesh and has no comparison value so it was left out in Fig. 33.

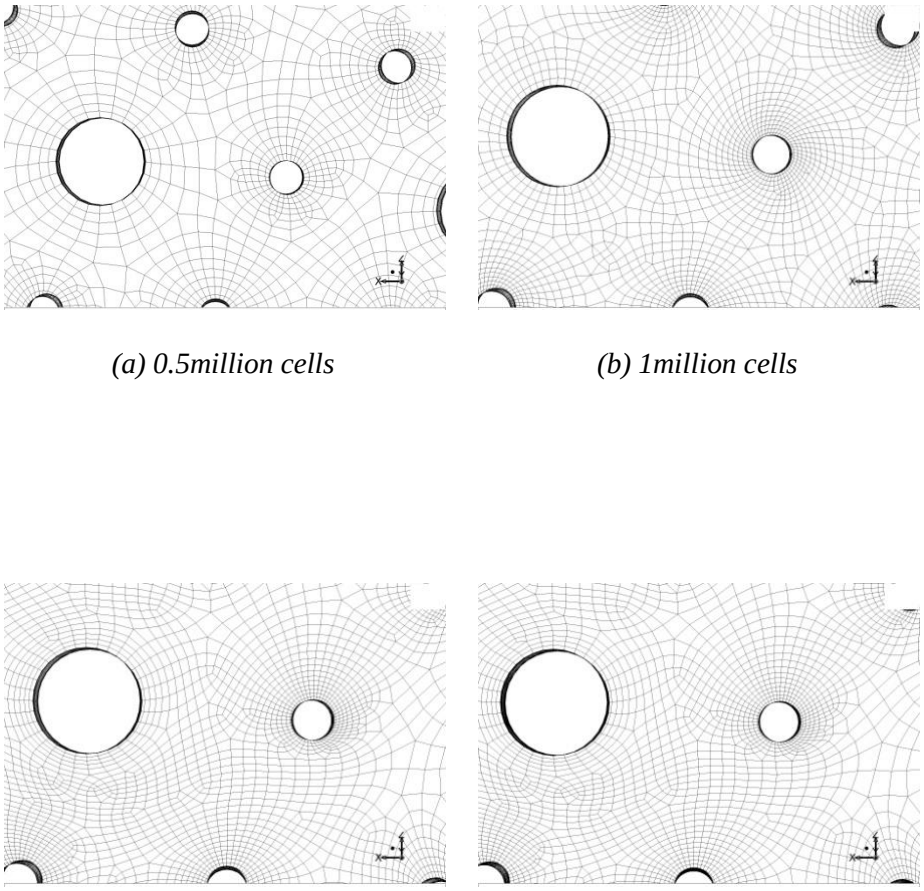

(a) 0.5million cells *(b) 1million cells*

(c) 2million cells *(d) 3million cells*

Figure 32. Top view of surface mesh refinement difference between mesh sizes of 0.5, 1, 2, and 3 million cells

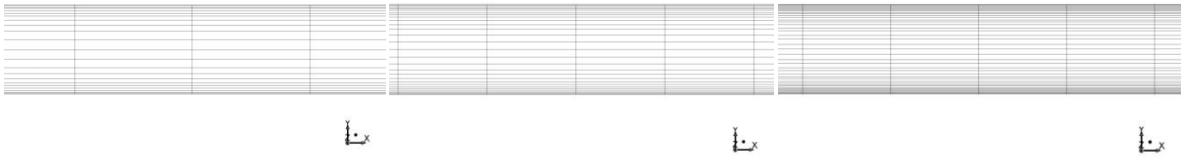

(a) 1million cells, 22 layers *(b) 2million cells, 28 layers* *(c) 3million cells, 42 layers*

Figure 33. Front view of symmetry plane showing gradient wall layers developed for mesh size of 1, 2, and 3 million cells

Difference in pressure drop and average heat transfer coefficient between mesh sizes were calculated using Eq. 13 and 14, respectively. Between mesh sizes of 0.5 and 1 million cells, the percent change in Δp was negligible, while $\bar{h}$ showed a difference of 9.3 %. For mesh sizes of 1 and 2 million cells, difference in $\bar{h}$ was 4.4%, and in Δp 8.2%. Between mesh sizes of 2 and 3 million cells, both $\bar{h}$ and Δp showed a difference of less than 1%. Fig. 34 shows plot for T_{out}, $\bar{T}_{wall}$, $\bar{h}$, and Δp varying with mesh sizes. Also, Fig.35 and Fig.36 show cross-sectional plot of velocity and temperature profiles, respectively, for variation in mesh sizes. Though no significant differences were observed in solutions for mesh sizes between 2 and 3 million cells, mesh of 3 million cells provided better resolute and more accurate solutions, especially for calculation of local wall temperature and heat transfer coefficient. Therefore, all values reported were performed using mesh size of 3 million cells.

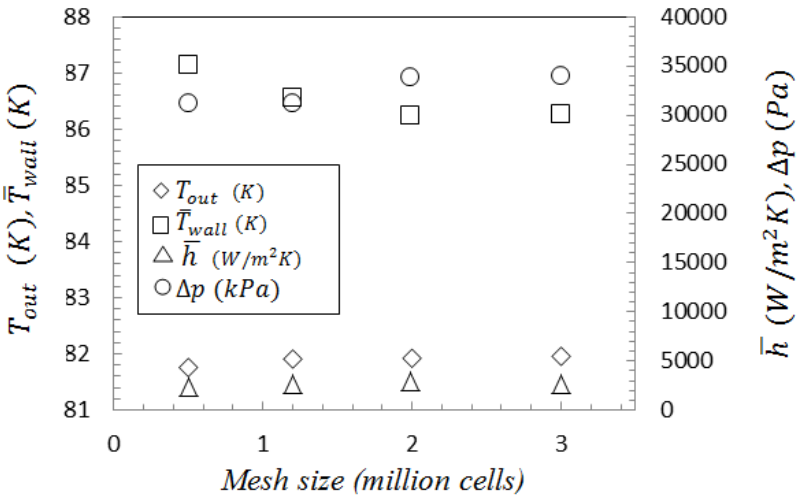

Figure 34. Variation of $T_{out}, \bar{T}_{wall}, \bar{h}$, and Δp with change in mesh sizes

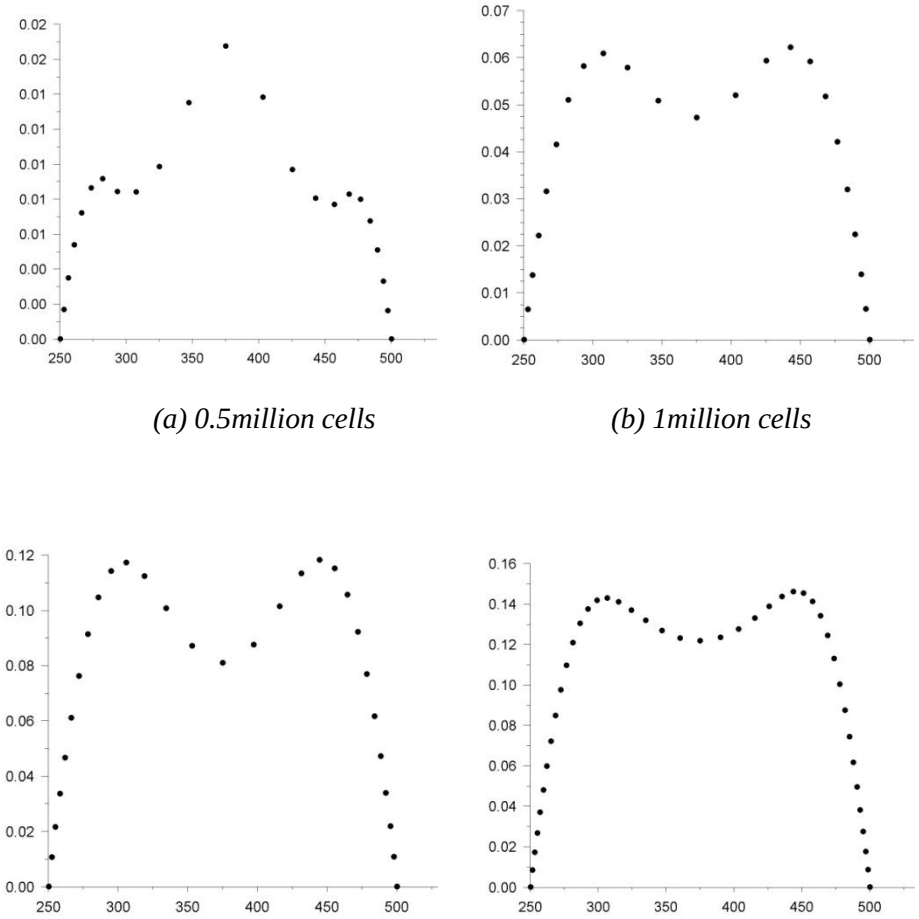

(a) 0.5million cells *(b) 1million cells*

(c) 2 million cells *(d) 3 million cells*

Figure 35. Cross-sectional velocity (m/s) profile shown in the vertical axis for the span of 250 micron height of the channel varied with grid refinement

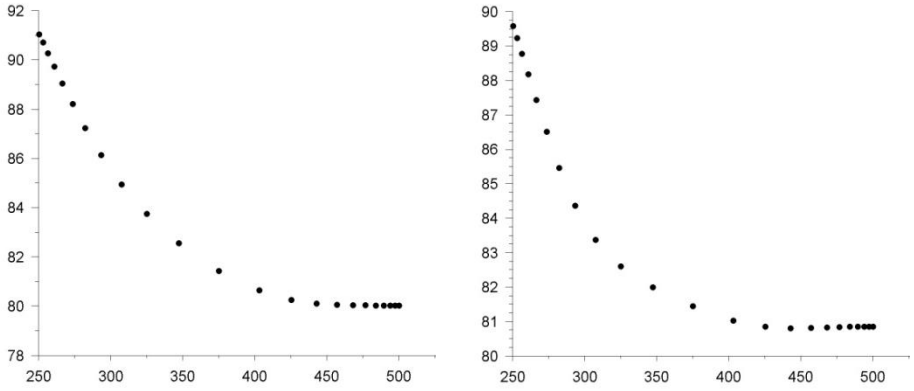

(a) 0.5million cells *(b) 1million cells*

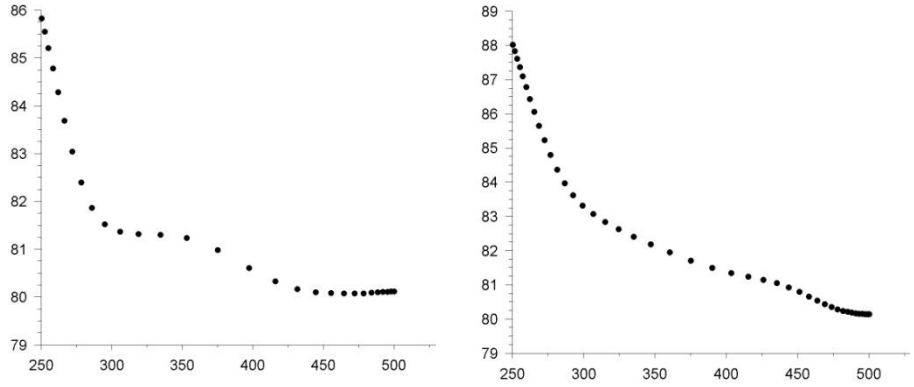

(c) 2 million cells *(d) 3 million cells*

Figure 36. Cross-sectional profiles of temperature (K) in the vertical axis for the span of 250 micron height of the channel varied with grid refinement

4.4 CFD DATA ANALYSIS- POST PROCESSING

Solutions from CFD simulations for pressure, wall and exit temperature for a range of mass flow rate and heat flux defined by the user were used to compute the pressure drop between the inlet and exit, and heat transfer coefficient.

Pressure was determined as the area-weighted average and given as,

$$\bar{P}_{num} = \frac{1}{A}\int P_{num} dA \tag{12}$$

where A is the surface area of the inlet or exit.

Pressure drop was taken as the difference between the inlet and outlet area-weighted average pressure,

$$\Delta P_{num} = \bar{P}_{num,inlet} - \bar{P}_{num,outlet} \tag{13}$$

The average heat transfer coefficient was calculated using Newton's law of cooling with values obtained from numerical results as,

$$\bar{h} = \frac{q^{"}}{\bar{T}_{wall} - \bar{T}_{bulk}} \tag{14}$$

where $q^{"}$ is the applied heat flux, $\bar{T}_{bulk}$ is the area-weighted average temperature between the inlet and exit.

The wall temperature was calculated as area-weighted average,

$$\bar{T}_{wall} = \frac{1}{A}\int T_{wall} dA \tag{15}$$

where A is the surface area of the heated wall.

In addition to obtaining an area averaged heat transfer coefficient, it is possible to analyze the local distribution using the detailed information presented in the CFD results. To quantify local heat transfer coefficient, h_{local}, Eq. 14 was used with the local values of the wall surface temperature, $T_{wall,local}$. These local temperatures were determined as

the temperature in the grid closest to the bottom wall. The bulk fluid temperature was taken as an average between the inlet and exit bulk fluid temperatures for all locations due to

the complexity of the geometry. The local heat transfer coefficient can be written as,

$$h_{local} = \frac{q''}{T_{wall,local} - \bar{T}_{bulk}} \quad (16)$$

5. RESULTS AND DISCUSSION

This section presents the experimental results of pressure drop and heat transfer rate, along with a comparison of the data with correlations in literature. Results of CFD simulations are then presented followed by a comparison between the experimental and simulation data on pressure drop and heat transfer coefficient.

5.1 EXPERIMENTAL RESULTS

Figure 31 shows the variation of average heat transfer coefficient, $\bar{h}$, and pressure drop, Δp, with mass flow rate, $\dot{m}$, over the range of the experiments. Recall that for a laminar flow condition in a channel of fixed geometry, the fully developed heat transfer coefficient is a constant and independent of flow rate. The estimated heat transfer coefficients, as seen in Fig. 37, shows a slight increase with increasing flow rate. However, noting the error bars, the increase is still within the uncertainty of measurements. The reason for the slight increase may be due to the developing nature of the flow and thermal boundary layer in the heat sink as well as due to the locations near the inlet and exit of the heat sink where the flow could potentially be turbulent (see Fig. 3).

Pressure drop is seen to increase with flow rate in range of test conditions. It should be noted that since pressure measurement uncertainty was low, the error bars are smaller than symbol size and hence do not appear in Fig. 37. With the exception of the last data point, the increase is linear with flow rate, which is to be expected for a laminar flow condition.

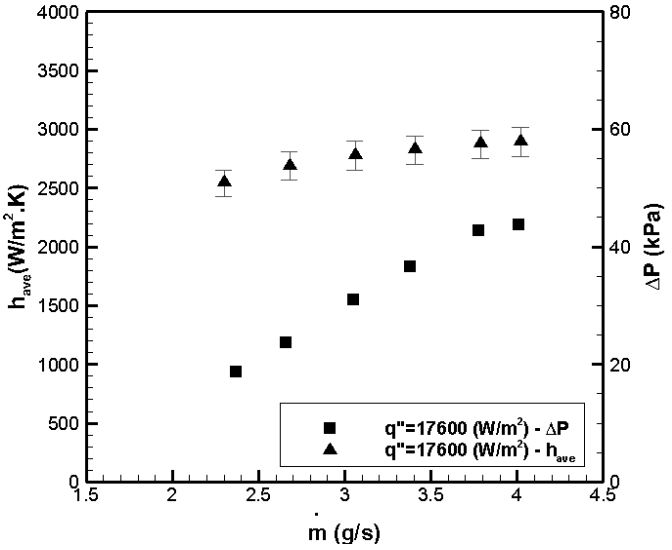

Figure 37. Average heat transfer coefficient and pressure drop variation with mass flow rate

Figure 38 shows the same data as in Fig. 37 but presented in a non-dimensional form, in terms of $\overline{Nu}$ and f varying with $\overline{Re}$. With an increase in $\overline{Re}$, it is seen that $\overline{Nu}$ increases. Previous studies on micro pin fins [9-11, 21] have indicated an increasing trend with Re for Nu and decrease for f with Re in the range of Re studied herein. However, the rate of increase of $\overline{Nu}$ with $\overline{Re}$ is lower for the present experiments compared with studies in literature while f remains constant until $\overline{Re}$ of 1100 and then exhibits a decreasing trend with further increase in $\overline{Re}$.

The present data were compared against selected correlations on cross flow over a bank of tubes and micro pin fin heat sinks from literature. These correlations are listed in Table 6 along with the range of parameters for which they were developed. Only a subset of available correlations is presented in the table based on the closest match of Re and pin height-to-diameter ratio range to the present experiments. In these correlations presented in Table 6, the Re is based on the pin diameter and the cross sectional average flow velocity. Because of the circular geometry of the current pin fin heat sink and the

variations in pin diameters, the Nu and f in the correlations were compared at the identical $\overline{Re}$, as defined in section 2.1. As indicated in Table 6, the tube bank correlations have as a geometrical parameter the transverse pitch, S_T, and longitudinal pitch, S_L, normalized by the pin diameter. Since there were three pin diameters in the present study, the number density averaged pin diameter was used in the correlations. Table 6 also shows the mean average error (MAE), defined as,

$$MAE = \frac{1}{N}\sum_1^N \frac{|\overline{\phi}_{exp} - \overline{\phi}_{pred}|}{\overline{\phi}_{exp}} \times 100\% \quad (17)$$

of the predictions by the correlations of the experimental data of f and $\overline{Nu}$.

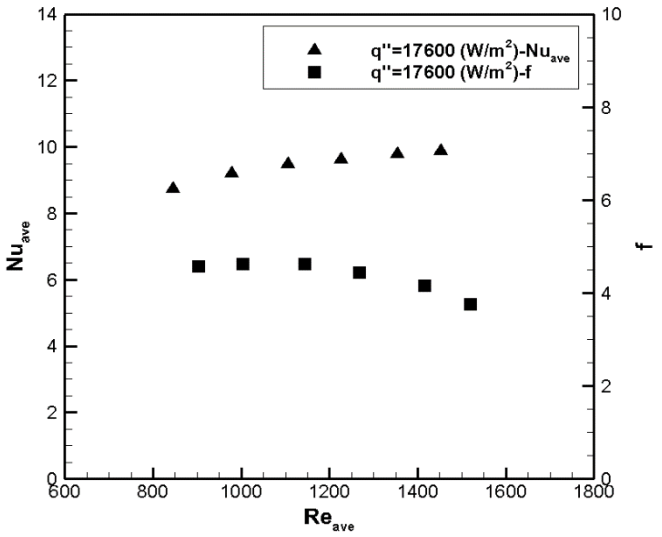

Figure 38. Average Nusselt number and friction factor variation with average Reynolds number

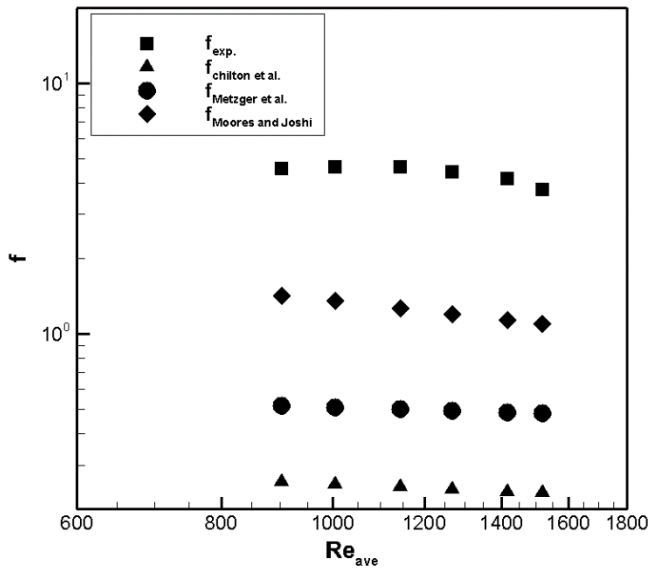

Figure 39, Comparison of average friction factor with predictive correlations listed in Table 6

Figure 39 compares the experimental results of friction factor, f, with correlations developed for $H/d > 8$ and $200 < Re < 20000$ by Chilton and Genereaux [22], for $0.5 < H/d < 8$ and $10^3 < Re < 10^4$ by Metzger et al. [23], and for $0.5 < H/d < 1.1$ and $100 < Re < 1000$ by Moores and Joshi [13]. The present experimental results correspond to $\overline{Re}$ from 800 to 1500, which is within the range of the correlations. However, the ratio of H/D based on a number density average of the diameters is 0.3, which is lower than that considered in any correlation.

Table 6. Correlation for friction factor and heat transfer in pin fin heat sinks

Reference	Remarks	Single-phase friction factor	MAE (%)
Chilton and Genereaux [22]	Tube bank Circular long tubes $1.2 \le S_T/d \le 5.0$ $1.0 \le S_L/d \le 2.5$ $200 \le Re \le 20000$	$f = \frac{3}{(Re)^{0.2}}$	94
Metzger et al. [23]	Pin-fin array $H/d = 1$ $1.5 \le S_T/d \le 5.0$ $S_L/d = 2.5$ $10^3 \le Re \le 10^4$	$f = 1.268Re^{-0.132}$	89
Moores and Joshi [13]	Micro pin-fin $0.5 \le H/d \le 1.1$ $1.3 \le S_T/d \le 1.36$ $1.13 \le S_L/d \le 1.18$ $200 \le Re \le 10^4$	$f = 19.04\left(\frac{H}{d}\right)^{-0.742} Re^{-0.502}$	71
Reference	Remarks	Single-phase Nusselt number	MAE (%)
Zukauskas [24]	Tube bank Staggered $S_T/S_L \le 2$	$Nu=0.35(S_T/S_L)^{0.2}\,\overline{Re}^{0.4}\,\overline{Pr}^{0.36}\left(\overline{Pr}_f/\overline{Pr}_w\right)^{0.25}$	195

Koşar and Peles [8]	Micro pin-fin $120 \le \mathrm{Re} \le 320$	$\mathrm{Nu}=0.0423\overline{\mathrm{Re}}^{0.99}\overline{\mathrm{Pr}}^{0.21}\left(\overline{\mathrm{Pr}}_{\mathrm{f}}/\overline{\mathrm{Pr}}_{\mathrm{w}}\right)^{0.25}$	480
Qu and Siu-Ho [12]	Micro pin-fin $\mathrm{Re} \le 250$	$\mathrm{Nu}=0.0241\overline{\mathrm{Re}}^{0.953}\overline{\mathrm{Pr}}^{0.36}\left(\overline{\mathrm{Pr}}_{\mathrm{f}}/\overline{\mathrm{Pr}}_{\mathrm{w}}\right)^{0.25}$	185

The correlation by Chilton and Genereaux [22] was developed for long tubes such that end effects were not significant. The correlations by Moores and Joshi [13] and by Metzger et al. [23] were developed for cross flow across a bank of short pin fins; however, the ratio of the pin height to diameter is larger than in the present study. These correlations have a lower MAE in comparison with the Chilton and Genereaux correlation, albeit very large at 71 percent.

Figure 40 shows the comparison of the experimental data against correlations of $\overline{Nu}$with $\overline{Re}$ from $\overline{Re}$ of 800 to 1500. Alongside the data are plotted correlations by Zhukauskas [24], Kosar and Peles [7], and Qu and Siu-Ho [11]. The Zhukauskas correlation was developed for cross flow over a bank of tubes and is valid for $H/d > 8$. The correlations by Kosar and Peles [7] and by Qu and Siu-Ho [11] are specific to microchannel pin fin geometries and are valid for $0.5 \le H/d < 8$ and for $H/d \sim 3$ respectively. These two correlations are valid only for a Re of up to 320, while the present experimental data span a larger range from 800 to 1500. The difference between the experimental data compared to correlations is reported as percentage of MAE in Table 6. It is evident from Fig. 39 and from Table 6 that none of the correlations can predict the present experimental data. Zukauskas [22] and Qu and Siu-Ho [11] correlations predicted

with about the same MAE of 190% while Koşar and Peles [7] correlation was different by a margin of 480%.

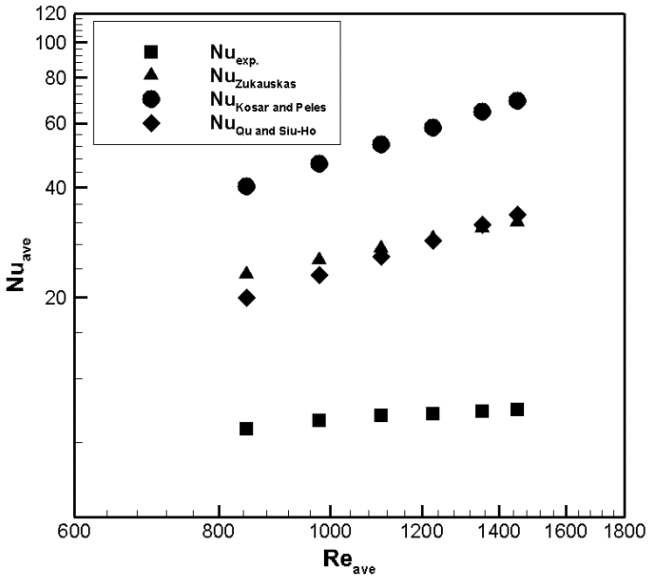

Figure 40. Comparison of average Nusselt number with predictive correlations

The large difference in pressure drop and heat transfer rate between the correlations in Table 6 and experimental data is likely a combined consequence of four factors: (a) the ratio of the pin height to average pin diameter is smaller than in the correlations, (b) the heterogeneity of pin diameters, (c) the non-standard transverse and longitudinal pitch to diameter ratios in the direction of the flow, and (d) the geometry of the heat sink, wherein the flow is distributed from the outer ring region to the region with the pins. A smaller pin height to diameter ratio essentially implies that the end wall effects due to boundary layer growth on the heat sink walls would have a significant effect on the flow and heat transfer rate. While the ratio of the radial and circumferential pitch to diameter ratio is fixed for this circular pin fin geometry, the transverse and

longitudinal pitch varies along the direction of flow within the heat sink as seen in Fig. 1. This pitch variation has a significant effect on the pressure drop and heat transfer rate, as is evident from the correlations in Table 6. The consequence of the outer ring region on the flow field is elaborated in the next section based on CFD results.

5.2. CFD SIMULATION RESULTS

Simulations were performed for conditions of laminar flow, steady-state, no-slip at the boundary walls, adiabatic at the top wall, and uniform constant heat flux imposed at the bottom wall. Initial conditions were specified based on experimental values used for a range of mass flow rate, inlet temperature, and heat flux. Solutions from simulations are tabulated in Table 7.

Table 7. Solutions from numerical model for a given flow rate and heat flux (go in order of increasing flow rates)

$\dot{m}(g/s)$	$q"\ (W/m^2)$	$DP\ (kPa)$	$T_{in}\ (K)$	$T_{out}(K)$	$T_{wall}(K)$	$h\ (W/m^2K)$
4.01	18515.31	50.817	78.08	81.60	85.60	3213.766
3.78	18638.1	45.475	77.77	81.50	86.70	2638.232
3.38	18529.9	38.151	77.57	81.74	86.03	2908.306
3.05	17450.06	30.871	77.62	81.96	86.27	2692.278
2.66	16721.61	24.349	77.63	82.43	86.71	2503.235
2.37	15707.99	18.362	77.59	82.88	87.14	2275.961

Fluid velocity magnitude contours and static pressure contours at the mid y- plane of the heat sink are shown in Figure $41a$ and b respectively for a representative mass flow rate of 3 g/s and an applied heat flux to the bottom wall of 17450 W/m^2. The inlet is located on the right side and the flow occurs from the right to the left. From the velocity contours in Figure $41a$, it is clear that a significantly higher velocity exists in the outer regions of the heat sink within the flow distribution ring formed by the tabs. Relatively higher velocity is also observed near the centerline, where flow from the tabbed outer region enters the pin fin region. Barring the center region, the velocity is nearly constant within the pin fin portion of the heat sink. The largest magnitude of velocity is seen at the inlet and exit. This is consistent with calculated Re_{local} along the x-direction shown in Fig. 3. The pressure contours in Fig. $41b$ indicates a region of high pressure at the inlet and fairly uniform pressure of between 45-50 kPa over a significant portion ($\sim 2/3rd$) of the heat sink.

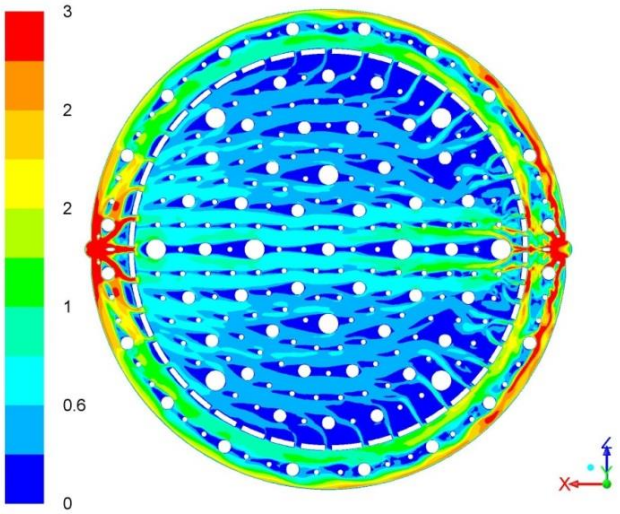

(a)

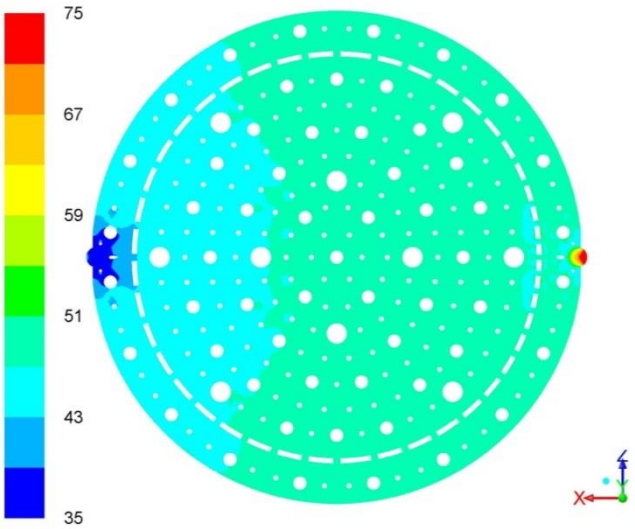

(b)

Figure 41. Contour maps of velocity magnitude (a) and static pressure (b) within the heat sink for a mass flow rate of $3\ g/s$ *and an applied heat flux to the bottom wall of* $17450\ W/m^2$.

Figures $42\ a$ and b present contour maps of the local heated wall temperature and the computed local heat transfer coefficient as outlined in Section 4.4 for the same flow condition as in the maps shown in Fig. 41. Commensurate with the larger fluid velocity in the outer regions formed by the tabs, the temperatures in these locations is also lower. Lower temperatures are also observed in the centerline region of the pin fin consistent with the higher velocities in this region. Local regions of high temperature are observed in the wake of the pins as well as some tabs.

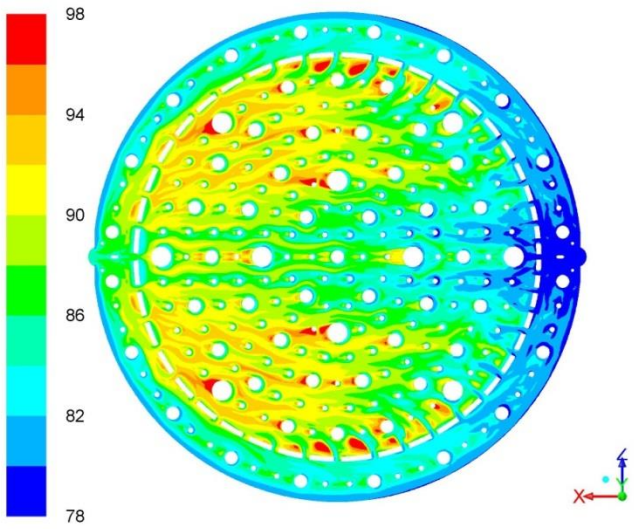

(a)

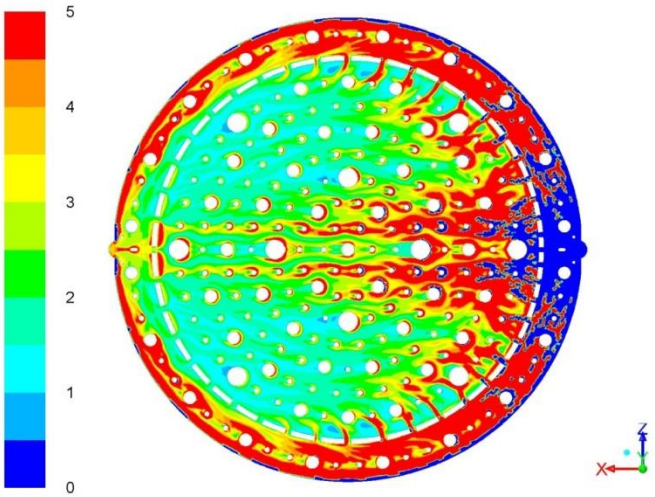

(b)

Figure 42. Contours of (a) wall temperature and (b) local convective heat transfer coefficient for a mass flow rate of $3\ g/s$ *and an applied heat flux to the bottom wall of* $17450\ W/m^2$.

The contour plot of local heat transfer coefficient in Fig. $42b$ shows significant variations at entrance and exit regions where the cross sectional area varies rapidly thereby causing rapid changes in local velocity. Consistent with the lower temperature

and higher velocities in the centerline region of the pin fin heat sink, the local heat transfer coefficient is higher in these areas as well as in the outer regions formed by the tabs. The design with the outer tabbed region for flow distribution was meant to eliminate the need for a dedicated plenum region for uniform flow distribution, thereby permitting simpler fabrication of the heat sink. From the simulation results, it is clear that this heat sink design can benefit from further optimization to permit a more uniform flow, and hence more uniform temperature distribution.

5.3. *Comparison of Experiments with Numerical Simulations*

Figures 43 and 44 depict plots of Δp and $\bar{h}$ comparing measured data to numerical simulation results for different average Re numbers at the same constant heat flux of $17{,}600\ W/m^2$. To report the difference between the measured data and values predicted from CFD simulations, the MAE has been calculated. For both quantities of $\bar{h}$ and Δp, numerical solutions were able to predict experimental data within 7.1% for $\bar{h}$, and 5.2% for Δp. The larger difference in pressure drop results from the last experimental data point. Nevertheless, the close agreement between the simulations and experiments is indicative of the fact that a majority of the flow within the heat sink is laminar. The agreement also supports the plausible reasons put forth in the previous section for the deviation between the experimental data and correlations in literature.

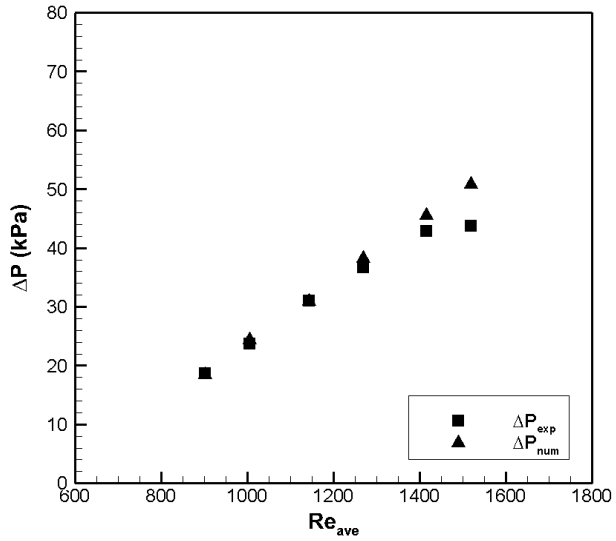

Figure 43. Comparison of average experimental and numerical pressure drop along the microchannel

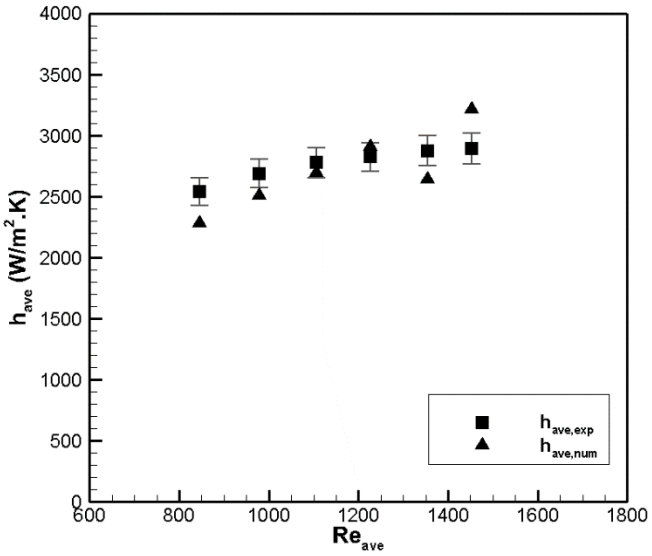

Figure 44. Comparison of average experimental and numerical averaged heat transfer coefficient

6. CONCLUSIONS

Cryogenic single-phase flow and heat transfer rate in a microscale pin fin heat sink was characterized using experiments and CFD simulations. Unlike other pin fin heat sinks, the one studied herein was circular in plan form, thereby creating a variable cross-sectional area along the heat sink in the flow direction. Other unique aspects of the heat sink included the circumferential plenum to distribute flow into the heat sink area and the heterogeneity in pin diameters. Results have been compared with existing correlations in literature. The findings can be summarized in following conclusions;

- Heat transfer coefficients were relatively unchanged at around $2600\ W/m^2 \cdot K$ with variation in flow rate between $2 - 4\ g/s$. Over the same range, pressure drop increased monotonically with flow rate.
- Comparison of experimental results for heat transfer and pressure drop with relevant correlations showed poor agreement. The lowest MAE for predicting Nusselt number and friction factor belongs respectively to Qu and Siu-Ho [12] and Moores and Joshi [13] with 185% and 71% deviation. The key reasons for poor predictions included the circumferential header, low aspect ratio of the fins, heterogeneity in pin diameters and the non-standard transverse and longitudinal pitch of the flow geometry.
- A 3D CFD model developed using ANSYS Fluent to predict the thermal and hydrodynamic characteristics of the heat sink. Results showed good agreement to corresponding experimental tests. The MAE of simulation for heat transfer coefficient and pressure drop were 7.1% and 5.2% respectively.

7. RECOMMENDATIONS

Redesign of the heat sink to improve fluid flow distribution is recommended. The velocity contour map in figure $41a$ shows fluid flow maldistribution from tabs of the circumferential plenum not being well spaced, with higher velocity around the plenum and along the centerline of the inlet and exit creating hot spot in regions with the lowest velocity. Figure $42a$ shows a contour map of the wall temperature with hot spot regions seen in area behind the pins opposite to the on-coming flow. The redesign of the heat sink would aim to eliminate hot spot regions by improving the flow distribution. Using CFD model, parametric study of variations in tabs and pin sizing along with density and spacing should be conducted. Keeping all else constant, each variable can be systematically studied to aid in the redesign of the heat sink.

On the experimental side, it is suggested that an alternative method to meter the mass flow rate in liquid form be developed to eliminate the pressure oscillation seen downstream of the flow resulting from the vaporization of LN_2 prior to the existing gas flow meter. This could be done, perhaps, by modifying a fluid meter with cryogenic compatible components.

8. NOMENCLATURE

A	Heat sink surface are (m^2)
A_c	Cross sectional are (m^2)
$\bar{A}_c$	Averaged cross sectional area along the microchannel used in Eq. 5 (m^2)
c_p	Specific heat at constant pressure ($J/kg \cdot K$)
d	Number density averaged pin fin diameter (m)
D	Diameter of heat sink (m)
D_h	Local hydraulic diameter (m)
$\overline{D}_h$	Averaged hydraulic diameter along the microchannel (m)
f	Friction factor
$\bar{h}$	Area-averaged heat transfer coefficient ($W/m^2 \cdot K$)
H	Height of micro pin fin (m)
k_f	Thermal conductivity of fluid at $\bar{T}_{bulk}$($W/m \cdot K$)
$\bar{L}_c$	Characteristic length defined in Eq. 5(m)
$\dot{m}$	Mass flow rate (g/s)
MAE	Mean absolute error
$\overline{Nu}$	Area-averaged Nusselt number
P	Pressure (Pa)
Pr	Prandtl number
Pr_f	Prandtl number at $\bar{T}_{bulk}$
Pr_w	Prandtl number at $\bar{T}_{wall}$
P_w	Wetted perimeter
q''_{net}	Heat flux based on heat sink surface area, A (W)
Q_{elec}	Heater power (W)
Q_{loss}	System heat loss (W)
Q_{net}	Net heater power goes through microchannel (W)
Re	Reynolds number
S_L	Longitudinal pitch of micro-pin-fins (m)
S_T	Transverse pitch of micro-pin-fins (m)
$\bar{T}_{bulk}$	Average bulk fluid temperature between the inlet and exit (K)
$\bar{T}_{wall}$	Average bottom wall temperature (W)

$\vec{v}$ Cross-sectional averaged velocity (m/s)

$\forall_{hs}$ Fluid volume within the heat sink (m^3)

x Distance from inlet of microchannel (m)

GREEK SYMBOLS

ΔP Pressure drop (Pa)

$\bar{P}_{num}$ Area-weighted average Pressure (Pa)

ρ Density (kg/m^3)

ν Kinematic viscosity (m^2/s)

$\emptyset$ Unspecified terms used in Eq. 17

SUPERSCRIPTS

$-$ Sign of averaged value

$\rightarrow$ Sign of vector

. Sign of rate

SUBSCRIPTS

$ave.$ Averaged value

$exp.$ Experimental value

$local$ Locally calculated

$num.$ Numerical value

9. BIBLIOGRAPHY

[1] Tuckerman, D. B., and Pease, R. F. W., 1981, “High-Performance Heat Sinking for VLSI,” IEEE Electron Device Lett., 2, pp. 126–129.

[2] Garimella, S. V., and Singhal, V., 2004, “Single-Phase Flow and Heat Transport and Pumping Considerations in Microchannel Heat Sinks,” Heat Transfer Engineering, Vol. 25(1), pp. 15-25.

[3] Colin, S., 2012, “Gas Microflows in the Slip Flow Regime: A Critical Review on Convective Heat Transfer,” Journal of Heat Transfer, Vol. 134, paper 020908-1.

[4] Tibirica, C. B., and Ribatski, G., 2013, “Flow Boiling in Micro-scale Channels-Synthesized Literature Review,” International Journal of Refrigeration, Vol. 36, pp. 301-324.

[5] Carlos A. Rubio-Jimenez, Satish G. Kandlikar, and Abel Hernandez-Guerrero, 2012, “Numerical Analysis of Novel Micro Pin Fin Heat Sink With Variable Fin Density” IEEE transactions on components, packaging and manufacturing technology, vol. 2, no. 5, pp. 825-833.

[6] J.F. Tullius, T.K. Tullius, Y. Bayazitoglu, 2012, “Optimization of Short micro pin fins in minichannels,” Int. J. Heat Mass Trans. 55, pp. 3921-3932.

[7] Koşar, A., and Peles, Y., 2006, “Thermal-Hydraulic Performance of MEMS Based Pin Fin Heat Sink,” ASME J. Heat Transfer, 128 (2), pp. 121–131.

[8] A. Koşar, Y. Peles, 2006, “Convective flow of refrigerant (R-123) across a bank of micropin fins”, Int. J. Heat Mass Transfer 49, pp. 3142–3155.

[9] R.S. Prasher, J. Dirner, J.-Y. Chang, A. Myers, D. Chau, D. He, S. Prstic, 2007, “Nusselt number and friction factor of staggered arrays of low aspect micropin–fins under cross flow for water as fluid,” J. Heat Transfer 129, pp. 141–153.

[10] A. Siu-Ho, W. Qu, F. Pfefferkorn, 2007, “Experimental study of pressure drop and heat transfer in a single-phase micropin–fin heat sink,” J. Electron. Pack. 129, pp. 479–487.

[11] W. Qu, A. Siu-Ho, 2008, “Liquid single-phase flow in an array of micro-pin–fins – Part I: heat transfer characteristics,” J. Heat Transfer 130 (122402).

[12] W. Qu, A. Siu-Ho, 2008, “Liquid single-phase flow in an array of micro-pin–fins – Part II: pressure drop characteristics,” J. Heat Transfer 130 (124501).

[13] Moores, K. A., and Joshi, Y. K., 2003, "Effect of Tip Clearance on the Thermal and Hydrodynamic Performance of a Shrouded Pin Fin Array," ASME J. Heat Transfer, 125, pp. 999–1006.

[14] C.A. Konishi, R. Hwu, W. Qu, F.E. Pfefferkorn, 2010, "Experimental study and numerical analysis of water single-phase pressure drop across a micro-pin–fin array," Proceeding of IHTC14-23171, Washington DC, USA.

[15] J.R. Mita, W. Qu, M.H. Kobayashi, F.E. Pfefferkorn, 2011, "Experimental study and numerical analysis of water single-phase pressure drop across an array of circular micro-pin–fins," Proceedings of ASME/JSME AJTEC2011-44583, Honolulu, Hawaii, USA.

[16] Carlson, D. M., Sullivan, D. C., Bach, R. E., and Resnick, D. R., 1989, "The ETA10 Liquid-Nitrogen-Cooled Supercomputer System," IEEE Transactions on Electron Devices, Vol. 36 (8), pp. 1404-1413.

[17] Anderson, J. C., Krane, R. J., Parsons, J. R., Bar-Cohen, A., 1992, "Optimization of the Thermal Design of a Cryogenically Cooled Computer," IEEE Transactions on Components, Hybrids, and Manufacturing Technology, Vol. 15 (5), pp. 794-805.

[18] Qi, S. L., Zhang, P., Wang, R. Z., and Xu, L. X., 2007, "Single-Phase Pressure Drop and Heat Transfer Characteristics of Turbulent Liquid Nitrogen Flow in Micro-Tubes," International Journal of Heat and Mass Transfer, vol. 50, pp. 1993–2001.

[19] Moffat, R., 1988, "Describing the Uncertainties in Experimental Results," Experimental Thermal and Fluid Science, 1(1), pp. 3-17.

[20] ANSYS Fluent 14.5 Theory Guide, 2012.

[21] Liu, M., Liu, D., Xu, S., Chen, Y., 2011, "Experimental study on liquid flow and heat transfer in micro square pin fin heat sink," Int. J. Heat Mass Trans. 54, pp. 5602-5611.

[22] T.H. Chilton, R.P. Genereaux, 1933, "Pressure drop across tube banks," Trans. Am. Inst. Chem. Eng., 1933, 29, pp. 61-173.

[23] D.E. Metzger, Z.X. Fan, W.B. Shepard, 1982, "Pressure loss and heat transfer through multiple rows of short pin fins," Proceedings of the 7th International Conference, Munich, West Germany, Volume 3 (A83-42700 20-34).

[24] Zukauskas, A., 1972, "Heat Transfer From Tubes in Crossflow," Advances in Heat Transfer, Vol. 8, Academic, New York, pp. 93–160.

APPENDIX A

Facility safety design

Prior to designing and constructing a cryogenic testing facility, extensive safety measures were considered and reviewed. A Failure Modes and Effects Analysis (FMEA) was performed on the test facility to identify the failure modes, their chance of occurrence, potential to detect failure in advance, and the severity if the particular failure mode were to occur. Table 3 presents a summary of the risk with larger numbers indicating higher risk. Details of each of the modes and the mitigation methods are presented following the table. In total, eight failure modes were identified and are listed in Table 8. Table 9 indicates the meaning of the numbered ratings identified in Table 8.

Table 8. Failure Modes and Effects Analysis

Failure Mode	Effects	Severity Rating (S)	Cause(s)	Occur-rence Rating (O)	Current Controls	Advance Detection Rating (D)	Risk Priority Number (RPN)
Toppling of the cryogenic tanks	Explosion that could damage the lab and potentially part of the building	10	Failure of mechanical connection to unistrut or failure of unistrut	1	Safety enclosure for the tanks; manual inspection of tanks prior to start of experiments	1	**10**

Leaks/burst in transfer hose lines/fittings	Potential to burn and physically injure operators if lines are flailing, potential damage to electronics	8	Leaks in fittings, over-pressurizing of lines, wear/fatigue of lines and fittings	5	Secure lines to unistrut frame; protective gear for operators; test for leak prior to day's experiment; replace fittings after a number of cycles; The best way to mitigate this mode is by using a solenoid valve on the cryogenic tank that can be shut using an emergency switch	8	**320**
Toppling of dewars	LN2 spill could cause potential burns to operator	4	Operator bumping against the table/dewar (table has wheels that if unlocked could result	1	Strap dewars to the unistrut; operators will ensure that the table is in locked position at all times; operators will	9	**36**

			in tipping)		wear safety equipment		
Electrical power failure	Causes liquid N2 to enter the flowmeter, causing damage. It could result in liquid exiting the bypass or flowmeter lines- which could cause freeze burns	3	Power failure	1	A normally closed solenoid valve will be placed upstream of the flowmeter and a normally open valve in the bypass line. In addition, coiled copper tubing will be used in the exit line past the bypass line so that liquid will have sufficient length to vaporize prior to the exit.	8	**24**
Loss of Liquid N2	Could cause overheating of the test section and gas flow into	1	The cryogenic-cyl tank or 160L Airgas tank run out of LN2	3	Ensure sufficient LN2 exists in both tanks prior to start of experiment; have a PID	1	**3**

	flowmeter				controlled power shut off to the variacs that control the test section and rope heaters. The temperature on the heated test section will be used as a sensor for the PID		
LN2 flows into the integrated test system	???	???	Operator forgot to switch components from integrated test to separate effects test	??	Strict adherence to operating procedures	2	
Leak of liquid N2 at the exit to the fumehood from bypass	Potential to burn operator; if it occurs in the flowmeter line,	3	Could occur during startup Failure of heaters, electrical failure, high	2	The line past the bypass solenoid valve will be made of uninsulated coiled copper tubing and will	1	**6**

line	damage to flowmeter		flow rate of fluid		be of sufficient length to ensure vaporization of liquid		
Operator in physical contact with cryogenic system components	Freeze burns	5	Could occur due to inadvertently touching cyro components especially during start up	1	All system components are thoroughly insulated; operators wear safety gear and adhere to operating procedures	1	**5**

Table 9. Failure Modes and Effects Analysis Legend

Severity Rating (S)	Meaning
1	Negligible Effect
2 to 3	Minor
4 to 6	Moderate
7 to 8	High
9 to 10	Very High (Results in unsafe operation)
Occurrence Rating (O)	Meaning

1	Negligible
2 to 3	Low (few failures)
4 to 6	Moderate (occasional failures)
7 to 8	High (repeated failures)
9 to 10	Very High (inevitable failure)
Advance Detection Rating (D)	Meaning
1	Negligible (certain detection)
2 to 3	Low risk (easily detected)
4 to 6	Moderate risk
7 to 8	High risk (unlikely detection)
9 to 10	Very high risk (almost undetectable)

Failure mode details

i. Toppling of cryogenic tanks

Such an event could be created by improperly securing the tanks to the unistrut frame or by failure of the securing mechanism. While failure of the securing mechanism on its own would not result in toppling, a lateral force such as that generated by bumping into the tank could cause the tank to topple. The consequences of such a failure are dire and could result in serious injury or death of the operators and severe damage to the laboratory and the building. However, the chances of such an occurrence are small. In

order to ensure that the failure mode is reduced, the following safety aspects have been incorporated into the experimental facility and procedures:

a. The two cryogenic tanks will be secured at two locations to the unistrut.

b. A unistrut frame will be placed all around the tanks to form a safety enclosure. This will prevent toppling of the tank even if the securing mechanisms have failed and the tank is bumped.

c. The start-up procedures clearly instruct the operator to check if the tank securing mechanisms are secure prior to testing.

ii. Leaks/burst in transfer hose/fittings

Thermal cycling, improper connection of fittings or over-pressurization could lead to leaks or a burst in the fittings or transfer hoses. Since liquid nitrogen is under pressure of up to $8\ bar$ within the system, a leak or burst is of great concern. A burst in the line could cause freeze burns to the operator. In addition, the lines could come loose and act as projectiles. Several considerations in the design and operating procedures have been incorporated to ensure that the chances of this occurrence are minimized:

a. All transfer hoses and dewars are securely held to the unistrut. The physical condition of the connections to the unistrut will be examined prior to the start of the day's experiments (prevents projectiles upon rupture)

b. Relief valves at $125\ psig$ have been placed on the cryogenic-cyl tank as well as just prior to the first transfer hose (prevents over pressurization)

c. All operators will be required to wear aprons, safety goggles, face shields, cryogenic gloves, and closed toed shoes prior to working with the system (prevents freeze burns due to leaks and bursts)

d. All fittings will be replaced through periodic inspection

e. Prior to experimentation, a leak test using nitrogen gas from the compressed gas cylinder will be performed to ensure connections are leak free. (prevents leakage/bursts due to improperly connected fittings)

iii. Toppling of dewars

Stability of the dewars that contain LN_2 is key to preventing spills and resultant freeze burns. Since the table on which the dewars are to be located has wheels, all dewars and hoses will be strapped to a non-moving laboratory frame provided by the unistrut. In addition, the table wheels will be locked. Safety gear will be worn at all times by the operators during testing.

iv. Electrical power failure

Two variacs provide electrical power to the test section heater and the line rope heater that is located upstream of the flowmeter. Electrical power is also needed for the flowmeter, pressure transducers and the data acquisition board and computer. In the event of an electrical failure, since the test section and rope heaters are inactive liquid would enter the flowmeter and potentially exit the system from either the bypass lines (if a power failure occurs during startup) or flowmeter line (if a power failure were to occur during continuous operation). There is a potential for the exiting liquid to splash causing

freeze burns and damage to surrounding electronics. While the severity of this failure mode is not high, several checks are in place to protect the operator and the equipment:

a. In order to protect the flowmeter from damage, a normally closed solenoid valve will be located in line and upstream of the flowmeter past the in-line heater. A normally open solenoid valve will be placed in the bypass line. In the event of a power failure, the liquid flow would then enter the bypass line and hence prevent flowmeter damage.

b. In order to prevent liquid exiting the system, coiled copper tubing will be used in the bypass line to ensure that sufficient heat is transferred into the tubing to cause evaporation of LN_2 prior to the bypass exit.

v. Loss of LN_2

If during the experiment, either the cryogenic-cyl or Airgas tanks were to run out of LN_2, the temperatures in the system would rise. The loss of liquid in the Airgas tank would result in vaporization of liquid in the HX and would result in gas flow through the downstream locations. This particular incident would not be a huge issue since gas low would cool the test section and downstream tubing. However, when the fluid in the tubing (supplied by the cryogenic-cyl tank) is exhausted, the test section and rope heater sections would get heated. While no catastrophic damage is expected, it is likely that the plastic headering within the test section could get damaged. In order to prevent loss of liquid during the experiment, operators should check the level of liquid in both cylinders prior to the start of the experiment. In order to prevent damage to the test section upon occurrence of such an event, a PID controller as well as a manual stop switch will be located prior to the variacs that power the test section and rope heaters. The PID

controller will obtain temperature input from the test section and be set to shut down if the temperature were to rise above $273K$.

vi. LN_2 flows into integrated test system

Since several components of this separate effects test facility are to be shared with the integrated testing facility, it is plausible that the operators could have forgotten to switch required components between the two experiments. No safety issues are anticipated in the event that the integrated test operator inadvertently lets LN_2 into the separate effects test facility. Strict adherence to the start-up procedures should prevent such an occurrence.

vii. Leak of liquid N_2 at the bypass exit

This mode can occur during start up or as a result of power failure. The mitigation methods are already discussed in the Electrical Power Failure section above.

viii. Physical contact with cryogenic components/splashing during boiloff

This safety hazard could occur due to boiloff of the liquid in the dewars during startup or if the operator were to touch the cryogenic lines in the test facility without use of safety gloves. Several safety aspects are incorporated in the system to prevent freeze burns:

a. The pressurized transfer hose lines are vacuum jacketed and can be touched with no burns.

b. The low pressure transfer hose that is used to fill the dewars and all fittings will be thoroughly insulated with layers of cryo-gel insulation.

c. The heat exchanger and test section are contained within dewars and are not accessible to the touch.

d. The dewars are covered with insulating lids to prevent splashing during boiloff.

e. The operators are required to wear all of the prescribed safety equipment prior to experimentation- namely- aprons, safety goggles, face shields, cryogenic gloves, and closed toed shoes.